

Chapter 1

Introduction

High energy physics probes the smallest scales in order to discover the fundamental constituents of the universe and how they interact. From these searches of the smallest scales, the standard model of particle physics has emerged. The standard model contains 3 forces, the weak, the electromagnetic, and strong force, and two types of matter that interact through these forces, quarks and leptons. The quarks can interact through all three forces. The leptons however only interact through the weak and electromagnetic force. The matter particles interact with each other through the three forces by exchanging the forces carrying vector bosons. Strong interactions take place by exchange of gluons, the weak by Z^0 and W^\pm bosons, and the electromagnetic by photon.

Each of these three forces emerges due to symmetries in the standard model. For example, the wave function of the Schrödinger equation is comprised of complex numbers. The standard model does not depend on the phase of these complex numbers. The phases for each of these numbers can be arbitrarily changed at all points in space and time without any changing the predictions of the theory. This is because the gradient of an arbitrary scalar field can be added to the \vec{A} , the vector potential, which gives rise to the electromagnetic without changing the magnetic field and electric field that ultimately interact with the particles. The invariance of the standard model to the complex phase of the wave function necessitates the existence of the electromagnetic force.

The standard model is made of the three such symmetries, each of which is described by a

gauge group. The $U(1)$ is the group that accounts for the electromagnetic interaction and gives rise to the photon. The $SU(2)$ group produces the weak bosons, Z^0 and W^\pm . The strong force mediated by the gluons are consequence of the $SU(3)$ symmetry of the standard model. Of these three groups two, $SU(2)$ and $SU(3)$, are non-abelian. The consequence of this, is that the W^+ and W^- can interact with Z^0 and photon, the gluons can interact with each other. Because the gluons can interact with each other in many more ways than the limited interactions between the W, Z and the photons, the non-abelian nature of the strong force is particularly pronounced.

The self-interaction of the gluons produces unique qualities of the strong force: confinement, and asymptotic freedom.

Microseconds after the big bang, the universe existed in a state known as the Quark Gluon Plasma (QGP). In the QGP, quarks and gluons are not in hadronic bondage, forced to the confines of bound states such as protons and neutrons. The Large Hadron Collider (LHC) produces QGP in the lab in PbPb (lead-lead) collisions. The high energies and rates of the collisions at the LHC make it possible to do detailed studies of the QGP. The LHC is producing rare experimental probes such as suppressed jets and heavy quarkonia at an unprecedented rate in heavy-ion collisions. Physicists now have better constraints on the properties like temperature, viscosity, and energy density of the QGP.

1.1 Theoretical Context

1.2 History

Chapter 2

The CMS Detector

CMS is housed at interaction point 5 of the LHC. The LHC is designed to pursue physics at the TeV scale. This is the scale where electroweak symmetry breaking is believed to occur [?]. While this means that the search for the standard model Higgs boson was the central driving design consideration, the wide range of possibilities for finding new physics signals requires a general purpose detector. The expedient discovery of new physics through low cross section interactions requires high luminosity. ~~This consideration leads inevitably to pile-up, where multiple collisions occurs at a single bunch crossing. At peak luminosity the LHC is expected to produce on average 20 hard proton-proton (pp) collisions per bunch crossing [?]. These particle physics considerations of high multiplicity due to pileup and the need for a general purpose detector make CMSserendipitously well suited for heavy ion physics.~~ While the difference in scale, 125 GeV for the mass of the Higgs boson as compared to 3.1 GeV for the mass of the J/ψ , create difficulties which will be discussed below, these two considerations created the opportunity to explore UPC J/ψ . Prior to the discovery of the Higgs boson, the decay $H \rightarrow Z^0 Z^{0*} \rightarrow \mu^+ \mu^- \mu^+ \mu^-$ because very few other process can create a four muon final state. Muon capabilities developed for this process can be used to study J/ψ , which also decays to muons. A versatile trigger is needed to accommodate the high interaction rates that accompany the high luminosities. By exploiting the versatility of the trigger and CMS's muon systems it is possible to explore process like UPC

58 J/ψ production, which push to the very edge of the detectors capabilities.

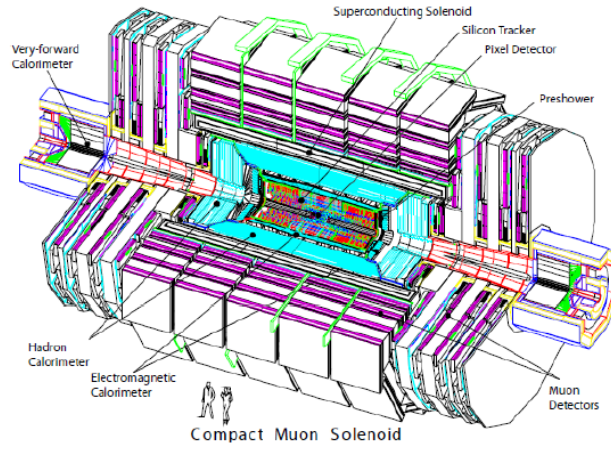


Figure 2.1: The Compact Muon Solenoid from Reference [?].

59 The general purpose design of CMS is dominated by the massive 4T superconducting solenoid
60 at its core. The magnets is 13m long with a 6m diameter, and pushes the limits of power and com-
61 pactness [?]. These two conflicting limits are achieved through the novel design of interweaving
62 structural and conducting elements together in the coil of the solenoid.

63 Within the solenoid resides three different sub detectors. The inner most is the world's largest
64 silicon tracker [?]. The tracker is surrounded by a highly effective lead tungstate crystal electro-
65 magnetic calorimeter (ECAL). ECAL is encapsulated in a brass scintillating hadronic calorimeter
66 (HCAL). Outside the magnet, muon chambers are used to aid in the measurement and triggering of
67 muon events. Altogether CMS weighs 12,500 metric tons, has a diameter of 14.6m, and a length
68 of 21.6m [?].

69 **2.1 Tracker**

70 The Silicon Tracker is the innermost sub-detector of CMS, and has active elements as close as
71 4.4cm to the interaction point [?]. The tracker has a length 5.8m, a diameter of 2.6m and covers
72 a range in pseudorapidity of $|\eta| < 2.5$. Pseudorapidity is defined as $\eta \equiv -\ln(\tan(\theta/2))$, where
73 θ is the polar angle, and ϕ is the azimuthal angle with respect to the beam axis. At the center

of the tracker are three rings of silicon pixels around the beam with two disks of silicon pixels to cap the rings. The pixel portion of the silicon tracker is comprised of 66×10^6 pixels. The silicon pixels are surrounded by silicon strips. The silicon strips are separated into 4 different sections: the Tracker Inner Barrel, the Tracker Inner Disk, the Tracker Outer Barrel, and the Tracker End Caps. The silicon strip detectors as a whole are comprised of 9.3×10^6 silicon strips. The high number of pixels and strips allow for the ability to distinguish and collect enough distinct points to reconstruct the path of the 1000 or so charge particles per bunch crossing expected at peak luminosity [?].

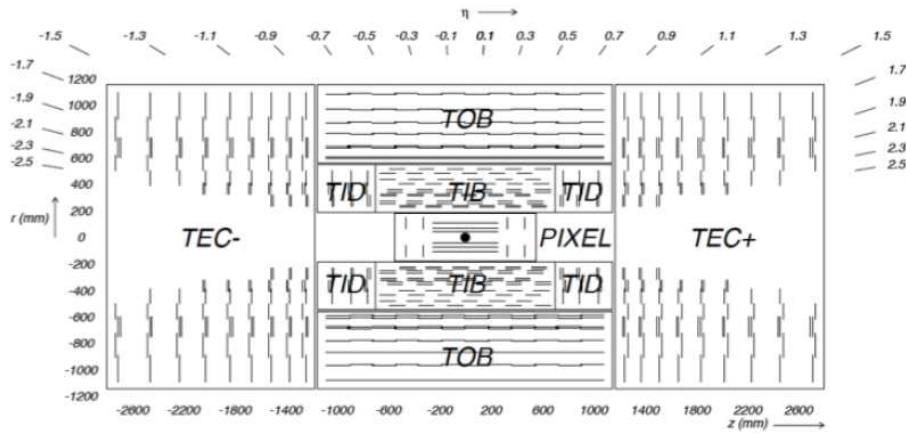


Figure 2.2: Layout of the silicon tracker with the pixels closest to the interaction point marked with a black dot and the strips segments beyond making up the remainder.

The amount of material present in the tracker is substantial enough to alter the path of particles as they pass through the tracker. Fig. ?? shows the amount of material in the tracker as a function of radiation lengths (X_0). The radiation length is the mean distance a high energy particle travels before giving up one e-fold of kinetic energy through electromagnetic interactions. For example, after one radiation length $E \rightarrow E/e$, where $e = 2.71828183$. As opposed to the deflection angle set by the strength of the magnetic field, momentum resolution for lower momentum tracks is limited by the lose of energy due to scattering of these particles off the material of the detector. For UPC J/ψ this is the primary factor contributing to the resolution of the reconstructed muon tracks.

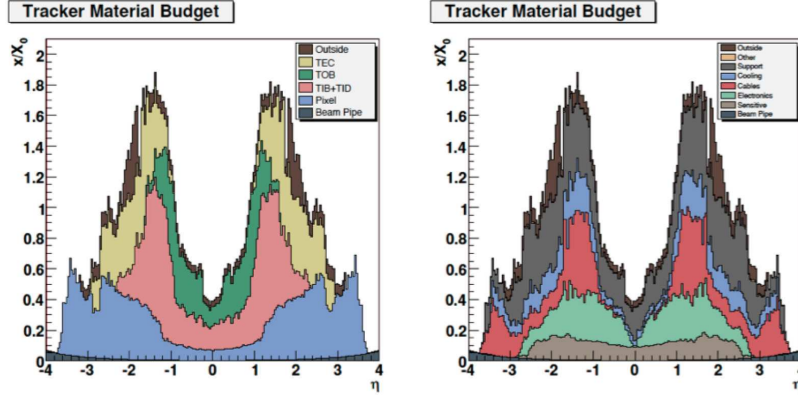


Figure 2.3: [Material in the tracker broken down by sub-detector\(left\) and category \(right\).](#)

2.2 [ECAL](#)

The next detector beyond the tracker is ECAL. ECAL is made of 61,200 lead tungstate (PbWO_4) crystals in the central barrel and 7,324 on each of the two endcaps [?]. The barrel (EB) covers a pseudorapidity range $|\eta| < 1.479$ and has an approximate $\eta - \phi$ segmentation of 0.0174×0.0174 . Lead tungstate is very dense, which is reflect in the high number of interaction lengths the short depth of one crystal provides. The crystals of the barrel have a depth of 230 mm corresponding to 25.8 ~~radiation lengths (X_0).~~ ~~The radiation length is the mean distance a high energy particle travels before giving up one e-fold of kinetic energy through electromagnetic interactions. For example, after one radiation length $E \rightarrow E/e$, where $e = 2.71828183$.~~ ~~The~~ [The](#) endcaps (EE) cover the pseudorapidity region $1.479 < |\eta| < 3$. In the endcap the crystals have an exposed area of $28.62 \times 28.62 \text{ mm}^2$, and a depth of 220 mm corresponding to $24.7 X_0$. The energy resolution of the ECAL as measured by test beam data can be seen in Figure ??.

2.3 [HCAL](#)

The HCAL like the ECAL has both a barrel (HB) and endcaps (HE). The pseudorapidity region $|\eta| < 1.3$ is covered by HB [?]. HB has an $\eta - \phi$ segmentation of 0.0897×0.0897 , and is 25 times more sparsely granulated than EB. HE covers the pseudorapidity region $1.3 < |\eta| < 3$. HE, like EE and the tracker endcaps, is aligned perpendicular to the beam axis resulting in granularity that

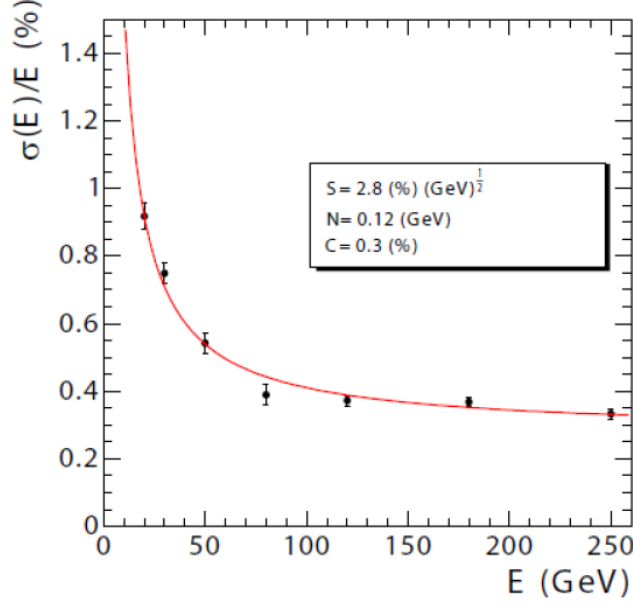


Figure 2.4: The energy resolution of ECAL as a function of energy from Reference [?].

changes with η . In the region $1.3 < |\eta| < 1.6$ HE has an $\eta - \phi$ segmentation of 0.0897×0.0897 . The $\eta - \phi$ segmentation roughly doubles to 0.17×0.17 in the region $1.6 < |\eta| < 3$. The energy resolution of the barrel and endcaps can be seen in Figure ?? . The thickness of the hadronic calorimeter is best described in interaction lengths, the mean distance for a particle to give up an e-fold of energy through nuclear interactions. At $\eta = 0$ the barrel has a thickness 5.82 interaction lengths (λ_I), and increases as the path length through the material increases to $10.6 \lambda_I$ at $|\eta| = 1.3$.

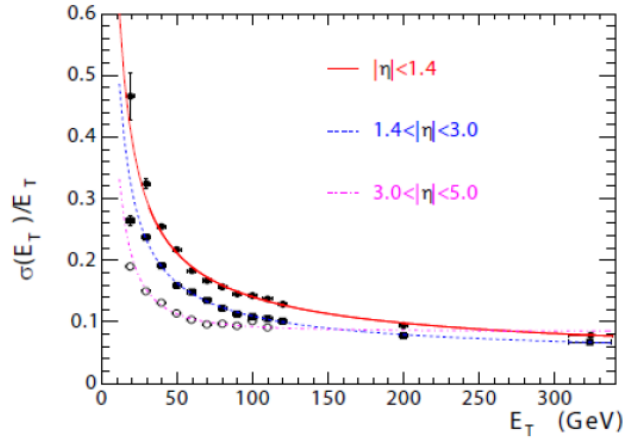


Figure 2.5: The E_T resolution of HCAL as a function of $|\eta|$ and E_T from Reference [?].

In addition to HB and HE, HCAL has two additional calorimeters. Because the space between ECAL and the magnet is restricted to 1.18 m, an outer hadronic calorimeter section (HO) is placed beyond the magnet in the region $|\eta| < 1.3$ [?]. The main function of HO is to collect energy from the highest energy hadrons before they reach the muon system. HO is not used in this analysis, but does contribute to the material budget. To increase the total calorimetric coverage, HCAL also has a quartz fiber calorimeter (HF) in the forward region, $3 < |\eta| < 5$. For the majority of HF's 13 η rings the $\eta - \phi$ segmentation is 0.175×0.175 . In the lowest $|\eta|$ ring the segmentation is 0.111×0.175 in $\eta - \phi$. In the highest two $|\eta|$ rings the segmentation in ϕ is 0.349, with an η segmentation of 0.175 in the outer and 0.300 in the innermost ring. The longitudinal direction is effectively segmented by using short fibers and long fibers. The measure energy deposited deeper than 22 cm is measured in both the short and long fibers, where as the long fibers are present throughout. This allows electromagnetic showers to be distinguished from purely hadronic showers [?]. The energy resolution for HF can be seen in Figure ??.

~~Beyond HF there are two more detectors in the forward region. CASTOR covers the range $5.2 < \eta < 6.6$ on the positive side of the beam. The~~

2.4 ZDC

Beyond HF, the Zero Degree Calorimeters(ZDC) covers the very forward rapidity region. ZDC sit between the beam pipes on either side of the interaction point covering the area around $\theta = 0$, $|\eta| > 8.3$. In heavy ion collisions the ZDC has the ability to measure neutral particles that do not participate in the collision [?]. ~~CASTOR extends the total coverage of the CMS as whole giving more access to low-x physics [?].~~

The ZDC has a total of 18 channels. Half of these 18 channels are on either side of the interaction point. The 9 channels on the side of CMS that correspond to positive η are denoted ZDC^+ , where as the 9 channels on the negative side are denoted ZDC^- . The 9 channels on each side are further sub-divided into an electro-magnetic (EM) section and a hadronic (HAD) section. The

EM section is positioned in front of the HAD section with respect to the interaction point and is segmented transverse to the beam direction. The 5 EM sections are positioned in front to absorb the energy from electro-magnetically induced showers, which develop over a shorter distance than hadronically induced showers. The transverse segmentation allows for a measurement of the transverse shower width and the size of the beam spot at the ZDC. The HAD section is segmented in the direction of the beam and consists of 4 channels. The longitudinal segmentation allows for absorption of the full extended hadronic shower and the ability to measure the longitudinal shower shape.

Each the 18 channels contains a tungsten target and quartz fibers. The dense tungsten target is used to initiate the shower. The quartz fibers shine Cerenkov light as the high momentum charged particles from the shower pass through it. the light from the quartz fibers is channeled to photo-multiplier tubes, one for each ZDC channel. Through a cascade of photon induced electrical discharges, the photo-multiplier converts the Cerenkov light to an electrical pulse.

This electrical pulse travels ~ 200 m down a coaxial cable from the LHC tunnel to the counting house in the CMS service cavern. There the electrical pulse is digitized by the Charge Integrator and Encoder (QIE). The QIE integrates the current each 25 nano seconds. The charge is than mapped logarithmically to the 128 bits. This bit is sent across a small fiber optic cable to the HTR firmware card. Here each 25 ns signal is stored in a 250 ns buffer, and the timing is sync with the rest of the detector to insure the ZDC signal arrives at the central data acquisition system at the same time as the other sub detectors from the same collision.

2.5 Muons

The muon system resides just outside of the superconducting magnet. It consists of three complementary systems: drift tube (DT) chambers in the barrel, cathode strip chambers (CSC) in the endcaps, and resistive plate chambers (RPC) in both the barrel and endcap regions [?]. ~~Ultimately the muon system is most useful for triggering on muons [?]~~ Each of the gaseous detectors function

in the same basic way. As the muon penetrates the gas volume electrons are knocked off of the gas atoms and these electrons are collected in the positively charged anode, where as the ionized gas moves to the cathode. The DTs in the barrel and the CSCs in the endcap have better spatial precision relative to the RPCs, which have are quicker and have more precise timing. The combination of the DTs and RPCs in the barrel and the CSCs and RPCs in the endcap allow for fast triggering and muon identification during data reconstruction.

The heavy-ion community is making use of the capabilities of CMS in a myriad of ways. The muon trigger has been used in the search for suppression of quarkonium states. This is an important probe of the correlation length within the hot dense state known as the quark gluon plasma (QGP)

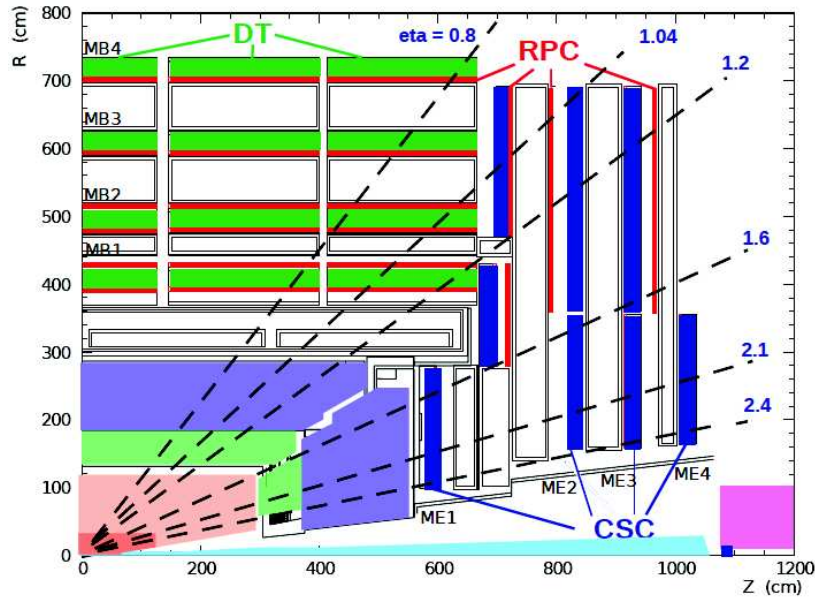


Figure 2.6: The CMS muon system showing the four DT stations in the barrel (MB1-MB4), the four CSC stations in the endcap (ME1-ME4), and the RPC stations.

As seen in Fig. ??, the DTs reside only in the barrel, covering the region $|\eta| < 1.2$. Consisting of a total of 172,000 cells, the DT cells are collected into 250 chambers. The DT chambers are in interwoven into the magnet field return yoke and are labeled by 5 segmentations in z , YB-2 to YB+2. Each z segment is divided into 12 ϕ segments labeled 1 at $\phi = 0$ and going to 12 rotating in positive ϕ with segments 4 and 10 contain 2 chambers. The segmentation in r is divided in to four parts, MB1-MB4. Fig. ?? shows how each chamber is made of three super layers. Super layers SL

178 Φ_1 and SL Φ_2 measure (r, ϕ) , whereas SL Θ measures z . The tracker has been utilized for to study
 179 charged particle multiplicities,

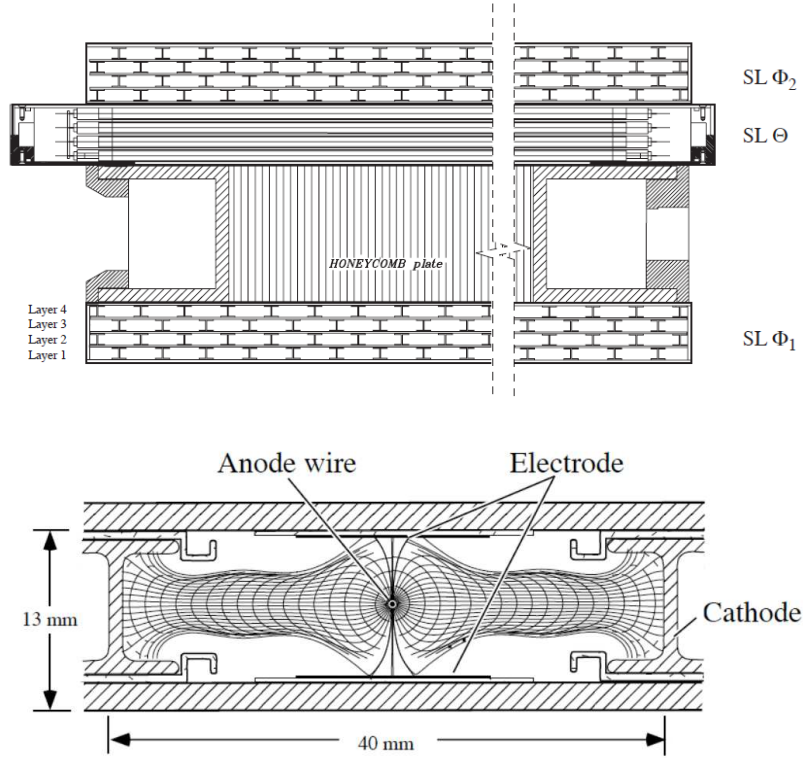


Figure 2.7: Schematic of the DT chambers and an individual DT cell.

180 The RPC complement the DTs in the barrel and the CSCs in the endcap primarily for the
 181 purpose of triggering. Six layers of RPC chambers are embedded in the barrel iron yoke, two
 182 located in each of the first and second muon stations (RB1, RB2) and one in each of the two last
 183 stations (RB3, RB4), where RB1 corresponds to r segment in the DTs MB1 and RB2 with MB2 etc.
 184 The redundancy in the first two stations allows the trigger algorithm to perform the reconstruction
 185 always on the basis of 4 layers, even for low particles, which may stop inside the iron yoke. In
 186 total there are 480 rectangular chambers, each one 2455 mm long in the beam direction. The strips
 187 run along the beam direction providing position measurements in the $(r - \phi)$ plane. In the endcap
 188 region, 3 layers of RPCs to cover the region up to $|\eta| = 1.6$. They are mounted on both faces of the
 189 disks. The double-gaps in every station have a trapezoidal shape and are arranged in 3 concentric
 190 rings in the $(r - \phi)$ plane. They overlap in ϕ to avoid dead space at chamber edges.

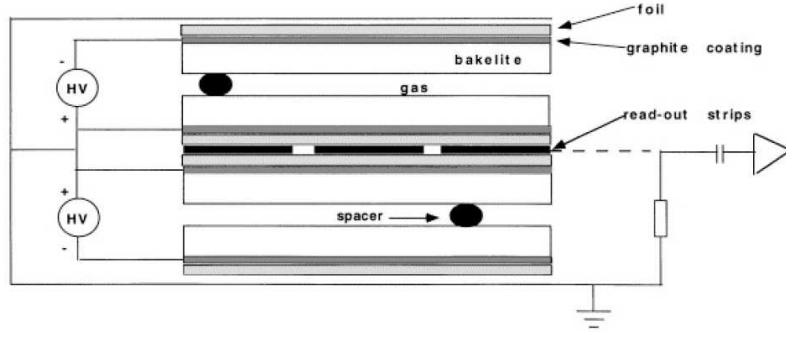


Figure 2.8: Schematic of a RPC cell.

The CMS Endcap Muon system will consist of 468 CSC arranged in groups as follows: 72 ME1/1, 72 ME1/2, 72 ME1/3, 36 ME2/1, 72 ME2/2, 36 ME3/1, 72 ME3/2, and 36 ME4/1. The chambers are trapezoidal and cover either 10° or 20° in ϕ ; all chambers, except for the ME1/3, overlap and provide contiguous-coverage. A muon in the pseudorapidity range $1.2 < |\eta| < 2.4$ crosses 3 or 4 CSCs. The CSCs are multiwire proportional chambers comprised of 6 anode wire planes interleaved among 7 cathode panels. Wires run azimuthally and define a tracks radial coordinate. Strips are on cathode panels and run lengthwise at constant $\Delta\phi$ width. The largest chambers, ME2/2 and ~~elliptical flow, two probes of~~ ME3/2, are about $3.4 \times 1.5 \text{ m}^2$ in size. The overall area covered by the sensitive planes of all chambers is about 5000 m^2 , for a gas volume more than 50 m^3 , and a number of wires of about 2 million. There are about 9000 high-voltage channels in the system, about 220,000 cathode strip read-out channels with 12-bit signal digitization, and about 180,000 anode wire read-out channels. This system will ensure at least 99% efficiency per chamber for finding track stubs by the L1 trigger and at least 92% probability per chamber of identifying correct bunch crossings by the L1 trigger. This efficiency per chamber and 3-4 CSCs on a muon track path, ensure that the reconstructed muons will be assigned the correct bunch crossing number in more than 99% of cases. The CSC system guarantees a $(r-\phi)$ resolution at the L1 trigger of about 2 mm, that improves up to $75 \mu\text{m}$ in off-line reconstruction for ME1/1 and ME1/2 chambers and about $150 \mu\text{m}$ for all others.

The primary function of the muon systems are to allow for triggering on and identification of muons. The tracker is still the primary instrument for measuring the muons. Fig. ?? shows

the resolution of reconstructed muons with the thermal expansion of the QGP. HCAL has aided in measuring jet suppression, which probes the strength with which the QGP interacts with strong interacting objects. Through its general purpose design and its ability to handle the high multiplicities produce by the LHC, CMS proves to be an excellent detector for investigating strongly interacting mater through heavy ion collisions. tracker only is only improved upon for muons with momenta above 100 GeV. For UPC J/ψ events where muons momenta are between 1-2 GeV, the muon system does not provide any advantage in terms of improved resolution. The muon system does distinguish muons from other particles. Because of their increase mass relative to electrons, muons emit less bremsstrahlung, or breaking radiation, as it penetrates the inner layers of the CMS on it's way to the muon systems. Fig. ?? shows the amount of material traversed by particles traveling through CMS as a function of $|\eta|$. The total of nearly 10 interaction lengths between the interaction point and the muon chambers, ensures that hadrons like charged pions, which nearly exclusively decay to muons, are collected in the calorimeters before converting to muons. By eliminating backgrounds from both electrons and hadrons, the CMS muons system allows for identification of muons for both triggering and reconstruction.

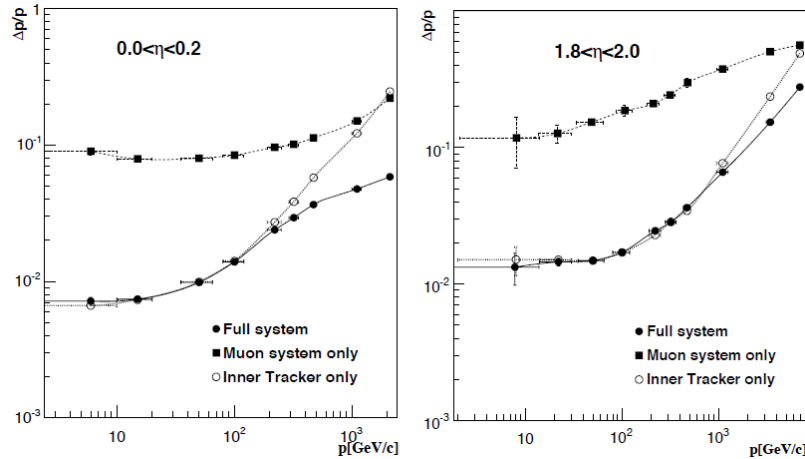


Figure 2.10: The momentum resolution of the muon system using only the tracker and the whole muon system in the barrel (left) and end cap (right).

The low-momentum nature of UPC physics creates complications due to the large amount of material between the interaction point and the muon systems. About 3 GeV of momentum is needed to reach the first layers of the muon system. In the rest frame of the J/ψ , the J/ψ equally shares its rest mass with its decay products creating 2 muons with momenta of about 1.5 GeV. For these daughter muons to reach the muon system, their parent J/ψ must be pushed to higher momentum by the initial particles which created the J/ψ . For this reason, muons from UPC J/ψ s are only detected at higher η values. Understanding this momentum restriction of the muon system was a major focus of the analysis discussed in this thesis with details described in Section. 1.6.

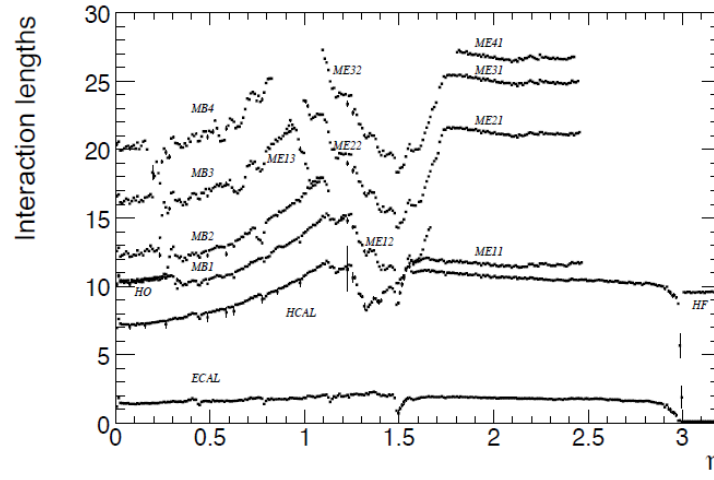


Figure 2.11: The amount of material in CMS as a function of η in number of interaction lengths.

2.6 Trigger

The CMS trigger is two tiered. The L1 trigger is the lower level hardware based system. The High Level Trigger (HLT) is software base and runs on a computer farm at point 5 where CMS is housed.

The purpose of the L1 trigger is to make quick decisions about which events will be kept temporarily for further processing. The L1 trigger is used to identify events where the tracker should be read out. Only the calorimeters and the muon system are used in the L1 trigger. Each of the sub-detectors has it's triggering hardware. The output from the sub-detectors is synchronized

to ensure that the signal from each of the sub-detectors comes from the same collision. The global trigger hardware then makes the final decision to initiate the HLT and to read out the tracker.

If an event passes the L1 trigger, the data from all the sub-detectors ~~in~~ including the Tracker are sent to the HLT computing farm. At this level the raw data from all the sub-detectors is unpacked and combined. The information from the calorimeters, muon system, and tracker can all be used to reconstruct basic physic objects in the HLT farm. For example, tracks can be combined with either ECAL energy clusters to form electron candidates, tracks can be combined with hits in the muon system to create muon candidates. At the HLT the whole detector is used together to select events. The raw data from the events that survive the HLT are recorded permanently, those that do not are lost forever.

The HLT farm must always be ready to accept events from the L1 trigger. For this reason, the amount of computing time each HLT trigger path uses must be balanced. For more rare L1 triggers, which will occur at a lower rate, more complex reconstruction software can be used. Conversely, simpler, faster, methods must be used for more common high rate triggers. Because of this time constraint in the HLT farm, the reconstruction algorithms used for triggering tended to differ from the final reconstruction algorithms. In the HLT these algorithms are optimized for quickness, whereas the final reconstruction is optimized for precision and accuracy. By having the ability to spend different amounts of computing time on different L1 triggered events, the complexity of the event selection offered by the HLT is heightened.

The two tiered triggering system creates very low dead times while maintaining purity and selectivity. During data taking the L1 trigger is continuously monitoring, and the HLT allows for sophisticated event selection. The wide gamete of physics topics that are pursued by the CMS collaboration are a testament to the effectiveness and versatility of the CMS two tiered triggering system.

Chapter 3

Analysis

In this chapter the various parts of the ~~measurements done for this thesis~~ analysis are explained. ~~The following chapter contains seven sections explain each of these parts: Monte Carlo simulation, trigger development, data sets and event selection, break-up determination, signal extraction, efficiency determination, and systematic checks.~~ In Section 1.1, the simulations used to estimate the ~~detectors~~ detector's ability to measure UPC processes are discussed. Section 1.2 explains the considerations that went into the triggers ~~which~~ that were developed for ~~the analyses discussed in this thesis.~~ ~~How the final events were selected and how triggers were used to separate the data in to data~~ this measurement. The event selection for the various data sets is detailed in Section 1.3. Extraction of the number of events from each of the three physics processes discussed in this thesis, coherent, incoherent, and photon-photon process ~~from the final selected events~~ is discussed in Section 1.5. The determination of the detectors efficiency for measuring UPC events is explained in Section 1.6. Finally, Section 1.7 lays out ~~how~~ the systematic uncertainties ~~are estimated~~ estimates on the measurements.

3.1 MC simulation

Every physical measurement is the product of the underlying physics folded with the response of the detector used to do the measurement. In order to understand the underlying physical process,

the detector's effect on the measurement must be understood and accounted for. As instruments become more and more complicated, the interplay between all of the many parts of the detector makes an analytic approach to the problem untenable. For this reason, the numerical technique of Monte Carlo (MC) simulation is the most useful approach.

MC simulations use random number generation to solve the problem numerically by brute force. First, particles are generated according ~~the~~ to theoretical distributions. These particles are then propagated through a simulation of the detector. As the particles pass through the detector, random numbers are again used to determine how these particles interact with the materials of the detector based on the known properties of the material. In this way, the theoretical distributions are ~~merged with the realistic response~~ convolved with a realistic model of the detector's response. A more detailed picture of how the detector shapes the underlying distributions with each successive event. The set of events that are produced resemble as closely as possible the results that would be seen were the physical process to be measured by the detector and physical process being simulated. ~~The collective combination of the many sub-detector responses with the theoretical distributions emerges from the successive creation of random events. The result is the convolved response of the detector with the underlying physical process that is to be studied.~~

In this thesis, two main classes of MC simulation samples were used. ~~The first class uses STARlight to generate events. This class of MC~~ , STARlight and a particle gun. The STARlight samples corresponds to the theoretical calculations described in Section ?? ~~. There are~~ , while the particle gun produces particles with a user defined momentum distribution. For STARlight three different physical process ~~described. Coherent~~ are simulated; coherent J/ψ production, where the photon couples to the nucleus as a whole, incoherent J/ψ production, where the photon couples to a nucleon within the nucleus, and ~~the~~ photon-photon ~~process~~ interactions, where the photons from the two nuclei interact with each other to produce a ~~lepton pair~~ pair of oppositely charge muons directly. All three STARlight samples ~~produce~~ contain a μ^+ and μ^- in the final state ~~that interacts with the detector~~. The second class uses PYTHIA6 to decay J/ψ s ~~with a given input produced with a user defined~~ p_T and rapidity distribution ~~. Two samples of this class of particle gun data were~~

produced each with different p_T distributions (See Fig.) into muon pairs.

Because STARlight is not integrated into the standard CMS software framework (CMSSW), a simulation software chain using STARlight was developed for the analysis described in this thesis. The software chain used for producing the STARlight samples has five steps. with 5 steps was developed. First, STARlight is run in the specified mode, and a single file is created for each physics process, for this thesis, one file for the coherent process, the incoherent process, and the photon-photon process for a total of three files. The output from the STARlight generator is in a format specific to STARlight, therefore, the output from the original generation step is then. In step 2 the STARlight output file is converted to the Les Houches (LHE) format. In this conversion to LHE format, either the $[\gamma]$, and the momentum of the parent J/ψ for the J/ψ production samples, or the initial photon-photon pair are added to the LHE output file. The standard STARlight output only includes record of each event. The event record produced by STARlight only contains the final state particles. Additionally, the initial output from STARlight is split into a collection of smaller LHE files so that each of the smaller samples can be processed in parallel. Each of the LHE files is

To process the events in parallel, the STARlight files are subdivided into in step 2, creating several LHE files from a single STARlight file. The LHE files are used as input to CMSSW. The three remaining steps Steps 3 to 5 take place within the framework. First CMSSW. In step three the generated particles are propagated through the GEANT4 $[\gamma]$ detector simulation. This accounts for all the interactions with the detector and produces as output a format identical to the raw data that is recorded during data taking. The next two steps are identical to Steps 4 and 5 are processed using the same software as in data taking. The In step 4 the reconstruction software used during data taking is run on the output of the detector simulation, and last, the The output of the reconstruction is reduced to the information that is needed for the final analysis in the final step.

The particle gun samples were created entirely within CMSSW. An interface to PYTHIA6 is included within CMSSW, which takes J/ψ mesons were created according to user defined p_T and rapidity distributions as input. The J/ψ are created according to the input distributions, and then

~~uses~~ PYTHIA6 ~~to decay~~ ~~[?]~~ decays the J/ψ s to μ^+ and μ^- . As with the STARlight samples, these muons are propagated through the GEANT4 simulation of the detector, and the raw data is produced. The remaining steps of running the reconstruction code and reducing the data to the final data needed for the analysis are identical to the STARlight production.

The ~~five MC samples~~ various MC samples, three STARlight samples ~~, and two particle gun samples,~~ differ primarily in the p_T distribution and the polarization of the J/ψ s produced ~~and the~~. The polarization of the J/ψ s, which effects J/ψ effects the angle at which the muon daughters are emitted relative to the direction in which the J/ψ is traveling. In Fig. ?? the p_T of J/ψ s from the coherent and photon-photon samples are peaked steeply a low p_T , and neither sample extends much beyond 0.15 GeV in p_T . The incoherent sample is peaked near 0.5 GeV and extends beyond 1 GeV. The two particle gun samples resemble the incoherent and coherent samples. The first sample has a Gaussian p_T distribution extending to approximately 0.15 GeV, whereas the second is flat in p_T up to 2 GeV. The particle gun samples are unpolarized, whereas the STARlight samples have transverse polarization. Therefore, the particle gun samples there is no preferred direction for the emission of the daughter muons. In the STARlight samples however the daughters tend to be emitted in line with the direction of the J/ψ 's momentum. This is particularly pronounced for the photon-photon process.

The momentum of the final state muons is the main drivers of whether the candidate can be measured. The polarization and the p_T distribution of dimuons from the generator determine the momentum of the daughters. The polarization effects how the momentum is shared between the daughters. In the rest frame of the parent particle from which the daughters decay, equal momentum is given to each daughter. However in the lab frame of the detector, the muon daughters which are emitted from transversely polarized J/ψ will tend to be emitted in the direction of J/ψ and will have unequal momentum in the lab frame ~~[?]~~. The daughter traveling in the direction of the J/ψ will have increased momentum, whereas the daughter traveling opposite to the J/ψ direction will have decreased momentum. The combination of these two effects create a muon with very low momentum compared to the typical momenta of muons measured by CMS. The

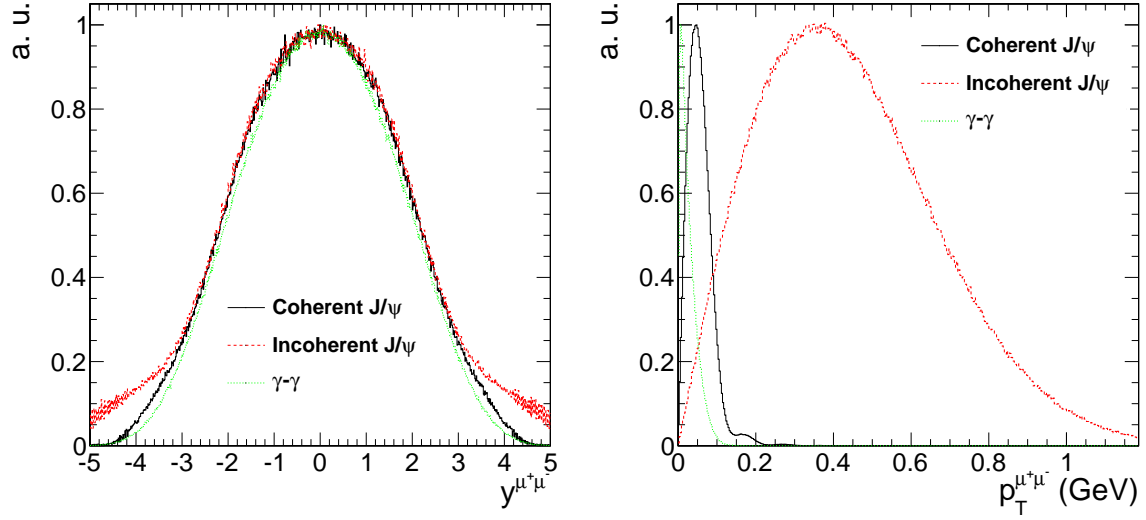


Figure 3.1: Generator level rapidity (left) and p_T (right) distributions for the coherent (black), incoherent (red), and photon-photon process (green).

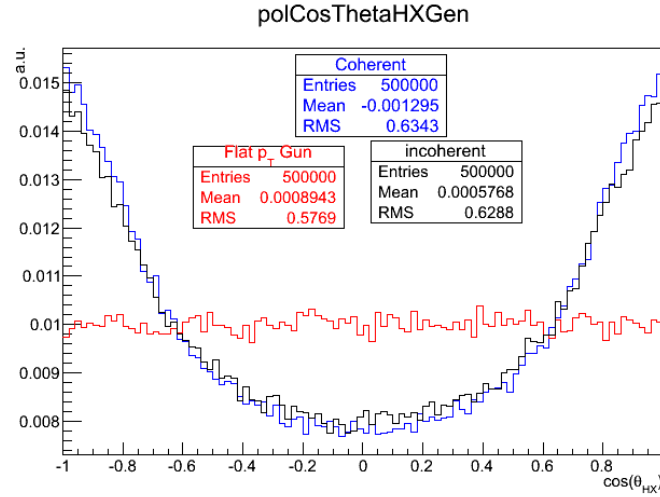


Figure 3.2: The J/ψ polarization of the particle gun (red), coherent (blue), and incoherent samples are plotted as the cosine of the helicity angle.

366 momentum of the lower momentum muon daughters is the main restriction on whether or not the
 367 J/ψ can be measured.

3.2 Trigger development

CMS collected dedicated UPC triggers for the first time during the 2011 PbPb run. Design of the UPC triggers required studies of the 2010 data to estimate rates and ensure that the bandwidth used by these trigger would be sufficiently low. All the different physics analyses must share the limited readout rate of the detector. For this reason, conservation of bandwidth was a major design consideration.

The 2010 rates were used to extrapolate to the interaction rate ~~of~~ expected prior to the 2011 ~~i~~ run. The unique UPC triggers were estimated by combining existing triggers from the 2010 run. By calculating the ratio between the UPC trigger rates and the minimum bias trigger rate, the UPC trigger rates were scaled up to the 2011 interaction rates using the 2010 data. The extrapolated rates allowed for ~~a package~~ the create of a package of triggers to be created that fit within the bandwidth requirement of CMS Heavy Ions group.

The trigger package for 2011 contained ZDC based efficiency monitoring triggers, muon and electron based triggers for measuring J/ψ , and backup triggers in case there was a problem with the original muon and electron triggers. In order to record the trigger efficiency monitoring data, the ZDC triggers had to be prescaled to a lower rate. The scaling down of the monitoring triggers were setup to insure overlap with the signal triggers. By balancing the competing objectives of rate reduction and increasing the overlap between the monitoring and signal triggers, the prescales for the trigger were as seen in Table ~~??~~ 1.1.

3.2.1 L1 trigger

The goal of the UPC L1 triggers was to record enough data to measure UPC J/ψ production via the dimuons and dielectrons ~~in-UPC events~~ channels. To achieve this, the loosest muon ~~trigger and~~ lowest threshold ECAL and electron triggers were paired with a trigger on energy in the ZDC and a veto on energy in the BSC. Additional triggers that vetoed on energy in HF were commissioned in case radiation damage during the run reduced the sensitivity of ~~BSCs. The L1 package that was~~

constructed for the analysis of UPC J/ψ is presented the BSCs. These triggers are summarized in

Table 1.1.

L1 Trigger Seed trigger	Rate (Hz)	Prescale	Id	Type
L1 MuonOpen and (ZDC ⁺ or ZDC ⁻) and BSC veto	2.1	1	1	Physics
L1 ECAL2 and (ZDC ⁺ or ZDC ⁻) and BSC veto	1.8	2	2	Physics
L1 ECAL5 and (ZDC ⁺ or ZDC ⁻) and BSC veto	0.3	1	3	Physics
L1 (ZDC ⁺ or ZDC ⁻)	Monitor L135	1500	4	Monitor
L1 MuonOpen and (ZDC ⁺ or ZDC ⁻) and HF veto	0	off	5	Backup
L1 ECAL2 and (ZDC ⁺ or ZDC ⁻) and HF veto	0	off	6	Backup
L1 ECAL5 and (ZDC ⁺ or ZDC ⁻) and HF veto	0	off	7	Backup

Table 3.1: List of 2011 L1 seeds.

The cumulative L1 trigger rate for all the UPC L1 trigger seeds was required to be 200 Hz. This requirement stemmed from the need to keep the tracker read-out rate low. The trackers baseline voltage can fluctuate due to the high tracker hit multiplicities in PbPb collisions. In order to monitor the zero suppression of the tracker, the zero suppression algorithm was executed using the HLT computing farm rather than in the tracker firmware. The rate at which the tracker could be readout without zero suppression set the limit for the L1 bandwidth.

3.2.2 HLT trigger

As opposed to the L1 trigger, which ~~reads-out the tracker~~ has access only to information from calorimeters and muon chambers, the HLT has access to ~~the tracker information~~ all the sub-detectors including the tracker. Reconstruction of a track in the pixel detector is used by the UPC paths. The use of the pixel detector only, as opposed to using the whole tracker including the silicon strip detector, allows for quick track reconstruction saving computing cycles. The requirement of at least one reconstructed pixel track for the HLT triggers was designed to reject backgrounds where no particles are reconstructed by the tracker.

The total HLT output for the UPC trigger package was 20 Hz. The limiting factor for the HLT rate was the amount of disk space available to store the data. To meet the bandwidth ~~the~~ requirements and collect a significant sample of data for estimating efficiencies, the prescales for

HLT Trigger trigger	Rate (Hz)	L1 prescale	HLT prescale	L1 seed	Type
HLT MuPixel_SingleTrack	<u>0.52</u>	<u>1</u>	<u>1</u>	<u>1</u>	Physics
HLT EG2Pixel_SingleTrack	<u>1.65</u>	<u>2</u>	<u>1</u>	<u>2</u>	Physics
HLT EG5Pixel_SingleTrack	<u>0.26</u>	<u>1</u>	<u>1</u>	<u>3</u>	Physics
HLT ZDC_PlusOrMinus	<u>3.6</u>	<u>1500</u>	<u>11</u>	<u>4</u>	Monitor
HLT ZDC_PlusOrMinusPixel_SingleTrack	<u>2.8</u>	<u>1500</u>	<u>1</u>	<u>4</u>	Monitor
HLT HfMuPixel_SingleTrack	<u>0</u>	<u>off</u>	<u>off</u>	<u>5</u>	Backup
HLT HfEG2Pixel_SingleTrack	<u>0</u>	<u>off</u>	<u>off</u>	<u>6</u>	Backup
HLT HfEG5Pixel_SingleTrack	<u>0</u>	<u>off</u>	<u>off</u>	<u>7</u>	Backup

Table 3.2: List of 2011 HLT trigger.

the triggers were set. ~~The~~ As an example of the balancing of the prescales, the ZDC trigger that was passed through from the L1 was given a ~~larger prescale to account for the higher rate relative to the more selective ZDC path, which~~ additional prescale factor of 11 on the HLT. The ZDC path ~~that~~ also required a pixel track on the HLT, ~~which~~ used the same L1 seed, was only prescaled at the L1. The prescale of 11 was set to ensure that a large enough sample of the pixel track ZDC triggers overlapped with the ZDC L1 only triggers so that efficiency of the pixel track requirement in the trigger could be estimated from the tracks lost. The prescale on the ZDC triggers were set to minimize the over all rate from the ZDC triggers all while ensuring a precision of 1% from the statistical errors from the efficiency measurement.

3.3 Event selection

In order to investigate novel physics processes like UPC J/ψ production, the LHC has delivered unprecedented amounts of data. The data for this analysis was recorded during the 2011 LHC PbPb run. During this period, $150 \mu b^{-1}$ were recorded by the CMS detector, corresponding to over a billion PbPb collisions. Of this, $143 \mu b^{-1}$ ~~are~~ were used in this analysis.

3.3.1 Data sets

Three specially selected samples were used for the present analysis ~~(, Physics, Monitoring, and Zero bias, see Table 1.3)~~. ~~By recording this hierarchy of samples, interesting events are selected~~

with a much higher purity in the physics sample, while the zero bias and ZDC triggered samples allow for the investigation of the selection criteria. These samples were recorded using subsets of the HLT triggers found in Table 1.2 of Section 1.2. The J/ψ events discussed in this thesis were obtained analyzing the sample labeled in Table 1.3 as physics. A ZDC triggered monitoring sample was recorded for the sake of estimating efficiencies. Last~~Last~~ly, a zero bias sample was recored for investigating the ZDC and the noise distributions of HF. ~~By recording this hierarchy of samples, interesting events are selected with a much higher purity in the physics sample, while the zero bias and ZDC triggered samples allow for the investigation of the selection criteria.~~

To record the physics sample containing the J/ψ signal, a muon trigger was paired with a veto on energy in the BSC and a requirement that there be energy in at least one of ~~two sides of the ZDC~~the two ZDCs. This trigger utilizes the unlikely chance of having overlapping noise in in the ZDC and muon detector. Because of the characteristically low momentum of UPC J/ψ as compared to J/ψ created by any other physics process, the loosest muon trigger was used. By pairing the muon trigger with the ZDC on the L1, the noise contribution was reduced from the noise contribution from either of the two sub-detectors to the noise coincidence between the two sub-detectors. Contributions from hadronic interactions are reduced by the veto on the BSC. In this way, the balance between reducing the rate and maximizing the efficiency was struck, allowing for the data to be recorded without producing high rates resulting in dead time for the detector.

In order to investigate the muon trigger and the other parts of the event selection, a minimum bias sample was recorded using the ZDC. For ZDC triggered sample, any event which had energy consistent with at least one neutron in either of the two sides of the ZDC was recorded. This process is much more common than the UPC J/ψ production. For this reason, the rates of this trigger are much higher than the physics trigger, and only a small sub set of these events are recorded. From this trigger the pixel track portion of the HLT trigger efficiency was estimated.

In addition to the minimum bias and physics sample, a zero bias sample was recorded to examine the ZDC trigger and the HF noise distributions. The zero bias trigger fired every time both beams passed through CMS. Only 4 events out of every million triggered were recorded for this

Sample	Events	\mathcal{L}_{int}
Physics	300K <u>346K</u>	143.3 μb <u>143.3 μb^{-1}</u>
Minimum Bias <u>Monitor</u>	100K <u>1.1M</u>	X <u>31.6 mb^{-1}</u>
Zero Bias	5M <u>8.8M</u>	580 b <u>580 b^{-1}</u>

Table 3.3: Integrated luminosities and number of events for the three samples used in this analysis.

sample. This sample allowed for an unbiased measurement of the ZDC trigger efficiency as discussed in Section 1.6. Because the zero bias trigger does not require any activity in any of the CMS sub detectors, the sample contains very few hadronic collisions. This allowed for a measurement of the electronic noise distributions in the HF, which will be discussed below.

The integrated luminosity for each of the three samples is calculated by recording activity in HF [?]. The cross section for HF activity is measured from a van der Meer scan, and the cross section was found to be X. In this way the amount of integrated luminosity for any running period is related to the activity in HF.

3.3.2 Event selection cuts

The analysis described in this thesis focuses on UPC J/ψ s decaying to muons. The trigger used for this analysis recored 346841 events. A set of off-line cuts were applied to increase the relative contribution of UPC events to background processes. Two sets of event selection cuts were applied to reject background events. The first set rejects background from the beam. The second rejects events where hadronic collisions have occurred. The cuts in Table 1.4 were applied.

To reject beam induced background the following cuts were applied:

- The reconstructed vertex must be within X cm in the transverse direction and X cm in the longitudinal direction. This cut insures that reconstructed particles come from interactions between the two beams rather than event where one of the two beams interact with gas particles near the interaction point.
- Beam halo muons were rejected using the timing of the muon hits. The beam halo cut rejects events where muons surrounding the beam stream through the detector.

cut cut <u>Cut</u> type	events <u>Cut</u>	<u>Even</u>
—	all triggered	— 3468
3*beam background rejection — —	good vertex requirement beam halo muon rejection cluster shape compatibility requirement	beam-background-r beam-background-r beam-background-r
3*hadronic interaction rejection — —	single-sided neutron requirement two track requirement HF signal rejection	hadronic-interaction hadronic-interaction hadronic-interaction
muon-quality-requirement fake muon rejection	1956 <u>muon quality requirement</u>	<u>204</u>
2*kinematic cut —	J/ ψ mass requirement muon detectability cuts	kinematic-cut kinematic-cut

Table 3.4: Effects of event selection cuts.

- Pixel cluster shape should be compatible with the vertex. This cut requires that energy deposits in the silicon tracker point back to the reconstructed primary vertex.

These beam background cuts do not reject any UPC J/ψ candidates.

The second set of background rejection cuts were designed to reduce contamination from hadronic interactions.

- No more than 2 reconstructed tracks in the event. The track requirement rejects events that produce many charged particles.
- Maximum reconstructed hit energy in HF was required to be below the threshold for electronic noise. Nearly all hadronic interactions (about 98%) produce particles in the range $3 < |\eta| < 5$ covered by the HF detector. By requiring that the energy deposits in HF resemble noise, nearly all elastic hadronic collisions are expected to be rejected.
- Energy in the ZDCs consistent with neutrons on only one side of the interaction point. In hadronic interactions both nuclei break-up. By requiring that ZDC only reconstruct neutrons on one side of the interaction point, hadronic interactions that produce neutrons on both sides were rejected.

Each of these cuts were designed to reject topologies produced by hadronic interactions. The effect of these cuts can be seen in Table 1.4 and are denoted hadronic interaction rejection.

To establish the HF noise thresholds, the noise distributions were measured in zero bias events. Only presences of both beams was required for these events to be recorded. An offline selection of events with no reconstructed tracks was used to ensure that no collision had taken place. The HF noise threshold was defined as the cut that keeps 99% of the zero bias events. The noise distribution from this zero bias sample is compared to the physics sample and MC in Fig. 1.3.

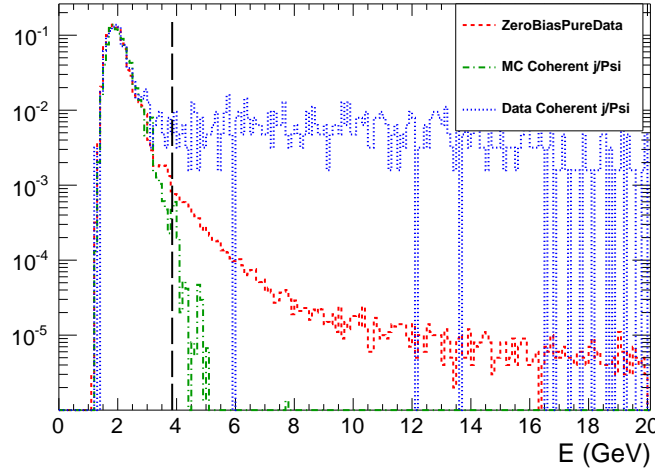


Figure 3.3: Comparison of HF noise distributions in zero bias data, physics triggered data, and MC.

The following standard muon quality cuts are applied:

- Tracker track matched with at least one muon segment (in any station) in both X and Y coordinates ($< 3 \sigma$).
- Cut on number of tracker layers with hits > 5 .
- Number of pixel layers > 0 .
- The χ^2 per degrees of freedom of the track fit < 3 .
- Loose transverse and longitudinal impact parameter cuts, with in 3 cm in the transverse direction and withing 30 cm in the longitudinal direction with respect to the primary vertex.

These cuts are applied to reduce the number of fake muons and have been validated for standard muon analyses.

3.4 Break up determination

As described in Section ??, UPC J/ψ photoproduction can be accompanied by the emission of neutrons from either of the two colliding nuclei. The various neutron emission scenarios, or break-up modes, can be distinguished by the ZDC. By separating events where the ZDC signal is consistent with 1 neutron versus several neutrons, the different break-up modes can be separated and compared to theory. For this reason, reconstruction of the ZDC signal plays an important role in this thesis. In order to maximize the ability to explore the one neutron peak, which sits at the bottom of the ZDCs dynamic range, a new ZDC reconstruction method was devised. This new reconstruction method was then used to establish a one neutron and many neutron threshold. In this section the ZDC signal reconstruction is described and how the neutron thresholds on this signal were set.

3.4.1 ZDC signal reconstruction

The ZDC signal is built up from the pulse shapes for each of the 18 individual ZDC channels. The pulse shape is recorded in 250 ns second chunks and is divided into 10 time slices of 25 ns (See Fig 1.4). Counting from 0, the 4th time slice is synced with the timing of the rest of the detector and corresponds to when the products of the recorded collision reached the ZDC. For this reason the channel signal is taken from the 4th time slice.

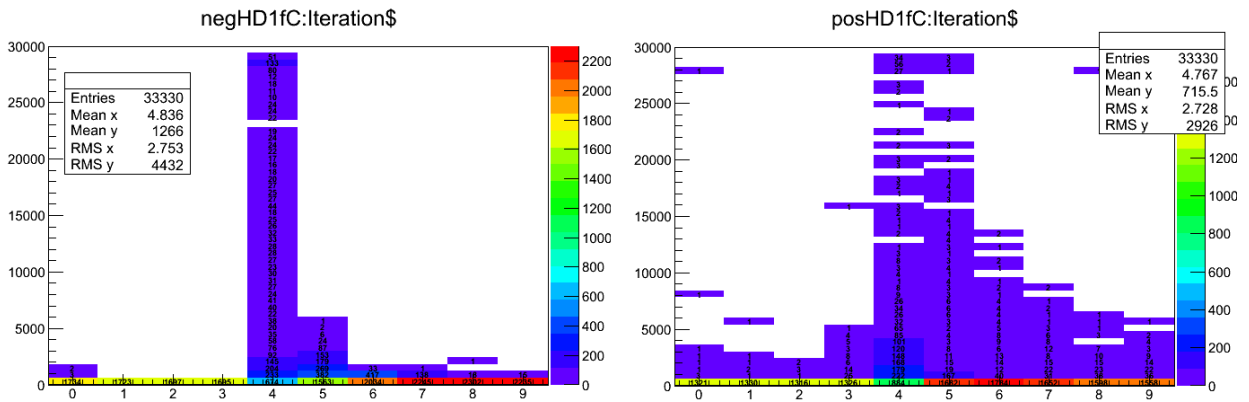


Figure 3.4: Average ZDC pulse shape is plotted as the charge as a function of time slice for the first hadronic from ZDC^- (left) and ZDC^+ (right).

The ZDC signal sits on top of a low frequency noise pedestal. Over the time scale of 250 ns, this low frequency noise signal appears as a constant that shifts randomly from event to event. The contribution from this noise is therefore measured event by event in order to subtract it. Time slice 5 is used for this purpose.

Time slices 1 and 2 could also be used to estimate the low frequency noise. However because the noise fluctuates to negative values of charge that cannot be measured, these time slices can only provide a measurement of the noise half the time. By using time slice 5 which contains the falling tail of the signal, the noise can be measured any time the signal raises significantly above the noise. If the fraction of signal in time slice 4 and 5 are constant and the noise contributes the same value to both time slices, the following formula is applicable:

$$Ts4 \propto (Ts4 + C) - (Ts5 + C) = Ts4 - R_{Ts5/Ts4} Ts4 = Ts4(1 - R_{Ts5/Ts4}), \quad (3.1)$$

where $Ts4$ is the signal contribution in time slice 4, $Ts5$ is the signal contribution to time slice 5, C is a random noise constant from the low frequency noise, and $R_{Ts5/Ts4}$ is the ratio between the signal contribution from time slice 5 over time slice 4. Fig. ?? demonstrates the consistence of the fraction and validates the unconventional method of using the falling tail of the signal to estimate the low frequency noise. By using time slice 5, the chances of measuring the noise are maximized. Separating the signal from the noise is especially important because the ZDC signal for the one neutron peak sits near the noise at the bottom of the ZDC dynamic range.

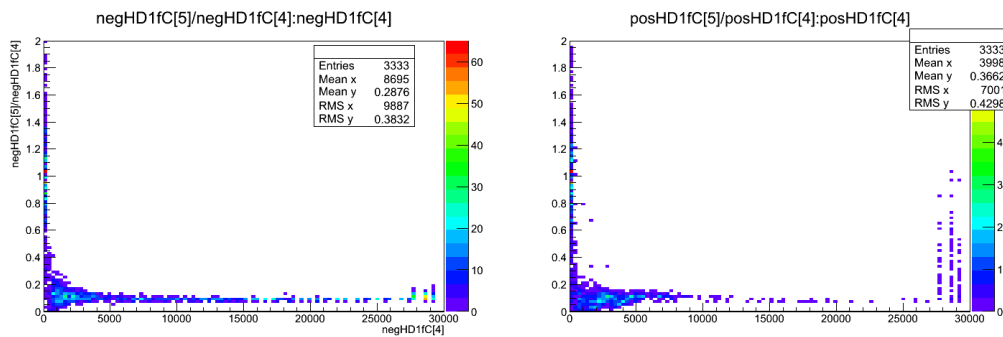


Figure 3.5: The fraction of signal in time slice 5 over time slice 4 as a function of the signal in time slice 5 in ZDC⁻ (left) and ZDC⁺ (right).

To measure one signal value for ZDC^+ and one for ZDC^- , the signals from each of the channels are combined. Channels from the EM section and HD section are combined first. Only channels with signal above zero in time slice 5 and time slice 4 are included. The EM section of the calorimeter is more densely packed with optical fibers and therefore has a higher gain relative to the HAD section. To account for this, the combination of EM channels is weighted with a factor of 0.1 to match the HAD channel gains. The value for each side of the ZDC's signal is given by the sum of the HAD channel combination and weighted EM channel combination. It is this signal, one for ZDC^+ and one for ZDC^- , which is plotted in Fig. ?? to measure the neutron thresholds.

3.4.2 Determination of the one neutron thresholds

The ZDC thresholds used to establish the various break-up modes were measured from zero bias data. By using this dataset, the neutron spectrum does not contain a trigger bias. Zero bias trigger required that both beams were present in CMS. This does, however, include a significant electronic noise contribution due to events where no neutrons are emitted in the direction of the ZDC.

To determine the thresholds for one and multiple neutrons, the ZDC^+ and ZDC^- spectra were fit. Four Gaussian functions were combined to fit the spectra. The electronic noise was fit to a Gaussian around zero. The one, two, and three neutron peaks are fit to Gaussians that are successively broader. The mean of each peak was initially set to multiples of the mean of the one neutron peak. The threshold for a neutron in the ZDC was taken from the fits in Fig. ?. Any signal greater than 2σ below the mean of the one neutron peak was considered signal. Any signal greater than 2σ above was considered multiple neutrons. In this way the single neutron break up modes could be separated from the multiple neutron modes.

Several of the break-up mode calculations that have been done involve single sided configurations where neutrons are present on one side of the interaction point and not the other. To identify signal consistent with noise, noise distributions for the combined EM sections and the combined HAD sections were measured. The beams are only made to collide every 200 ns. In Fig. 1.4 higher

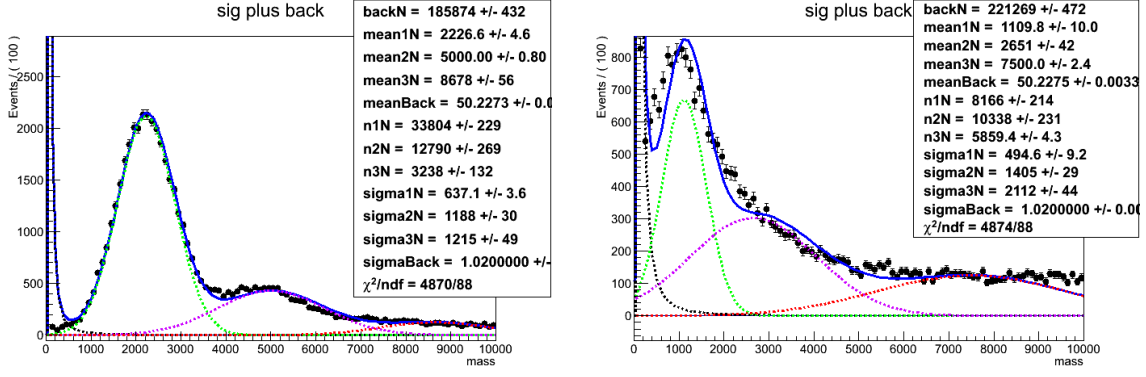


Figure 3.6: Fit to the signal spectra for ZDC⁻ (left) and ZDC⁺ (right)

than average signal can be seen in the 0th time slice, which precedes the main signal time slice time slice 4 by 200 ns. This is due to events where activity was present in the ZDC for two consecutive collisions. Time slices 1 and 2, however, occurred between collisions. These time slices were used to estimate the noise spectrum.

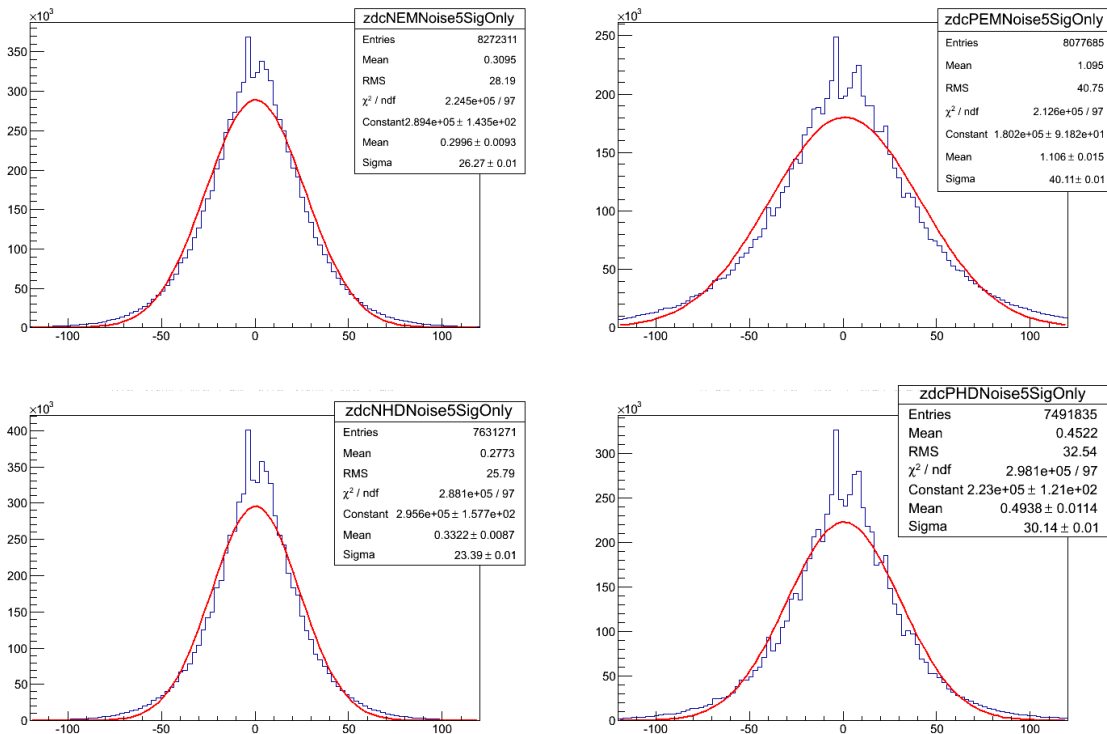


Figure 3.7: ZDC noise spectra from ZDC⁻ EM section (upper left), ZDC⁺ EM section (upper right), ZDC⁻ HAD section (lower left), and ZDC⁺ HAD section (lower right).

Fig ?? shows the noise spectrum for each of the EM and HAD sections for the two sides of the ZDC. As with the signal measurements, the low frequency noise pedestal is subtracted event by event by subtracting time slice 2 from time slice one before the channel signals are combined for each section. A side is considered consistent with noise if both HAD section and EM section signal measurements from the signal method involving time slice 4 and time slice 5 are lower than 2 sigma below the mean in Fig. ?. With the single neutron, multi-neutron, and noise thresholds established, the contributions to the various break-up modes were estimated and compared to theory.

3.5 Signal extraction

After all event selection cuts, the coherent J/ψ , incoherent J/ψ , and photon-photon process all contribute to the remaining events. Each process must be separated from the final mix. To achieve this, the invariant mass and p_T distributions are used to distinguish between the three processes. The photon-photon process is extended in invariant mass whereas the J/ψ is peak strongly near 3.1 GeV. In p_T the photon-photon and coherent process have similar distributions, both peaked shapely below 0.1 GeV, whereas the incoherent process is more broadly distributed across an interval extending to nearly 1 GeV. The mass distribution was fit to separate the photon-photon process from the J/ψ process. The p_T distribution was used to separate the incoherent process from the photon-photon process, and the coherent process. In this way, a separate yield was extracted for all three processes.

The invariant mass distribution for opposite sign dimuons is shown in Fig. 1.8. A J/ψ signal is clearly visible together with tails at higher and lower mass due to the photon-photon process. A fit to the invariant mass distribution was done using a Gaussian to account for the J/ψ signal and a first order polynomial function for the photon-photon process. The extracted number of J/ψ candidates from this fit includes all J/ψ s in the mass window that passed the analysis cuts, i.e. both coherent and incoherent process contribute to yield from the mass fit. The p_T distribution is

595 needed to separate the two different contributions to the J/ψ peak.

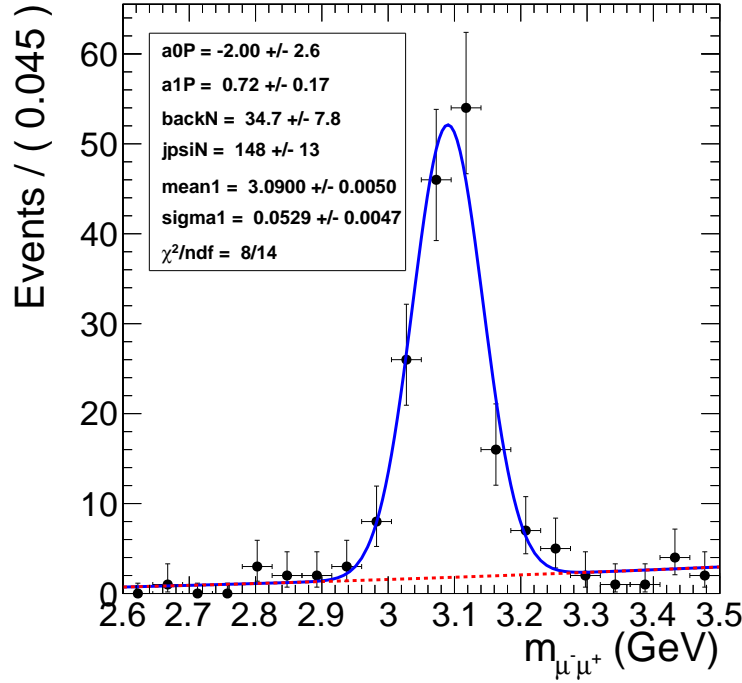


Figure 3.8: Mass fit to J/ψ using Gaussian for the signal and a first order polynomial for the photon-photon continuum

596 The same candidates from Fig. 1.8 were plotted as a function of p_T in Fig. 1.9. The clear
 597 overlap of the coherent and photon-photon process, and the clear separation of these two lower p_T
 598 processes from the incoherent process is apparent. The shape of the p_T distribution for the coher-
 599 ent, incoherent, and photon-photon process are taken from the final output of MC after applying
 600 all analysis cuts. To obtain the yields for each of the three process, the p_T distribution was fit to the
 601 three templates. In Fig.1.9, the yield parameters that were fit were left unconstrained for all three
 602 process.

603 The shape of the photon-photon and coherent J/ψ process are very similar in p_T . Accordingly,
 604 the contribution from the photon-photon process and the coherent process are difficult to separate
 605 from the p_T distribution. The confidence contours in Fig. 1.10 from the template fit in Fig. 1.9
 606 demonstrate the strong anti-correlation between the coherent yield parameter, nCo , and the yield
 607 parameter for the photon-photon process, $nGamma$. Because of the anti-correlation, the statistical

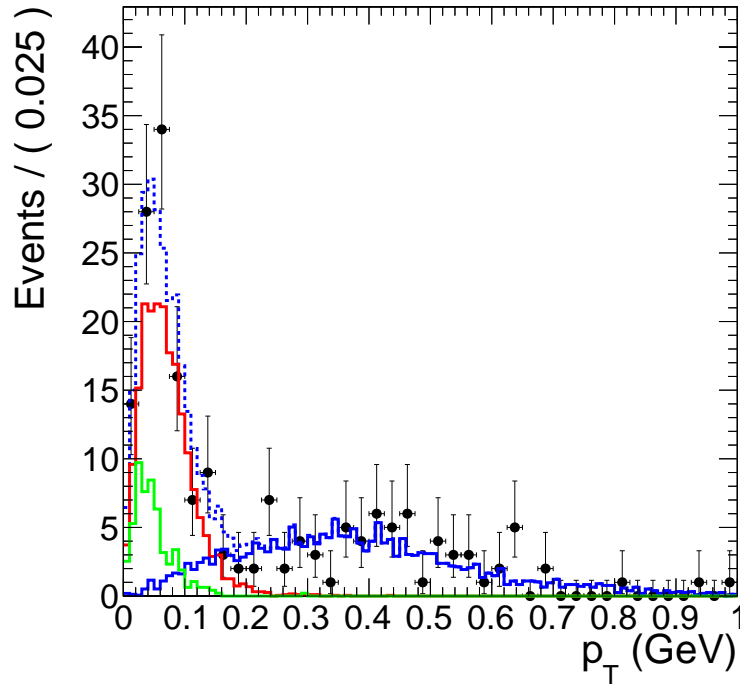


Figure 3.9: Fit to MC p_T templates.

uncertainty on nCo and $nGamma$ from the fit are larger than \sqrt{nCo} and \sqrt{nGamma} expected from Poisson statistics. The information from the invariant mass and p_T distributions were combined to break this correlation. Through this combination, the contribution to the final yield from the three process was measured.

To utilize the mass fits ability to distinguish the photon-photon process from the coherent and incoherent process all while utilizing the p_T fits ability to separate the coherent and photon-photon processes from the incoherent, a simultaneous fit to the mass spectrum and p_T spectrum was performed. Fig. 1.11 shows the result of the simultaneous fit. The simultaneous fit forces the parameter $nGamma$ to both describe the photon-photon continuum present in the side bands of the J/ψ mass peak as well the photon-photon contribution to the low- p_T part of the p_T spectrum. In addition, the J/ψ yield from the mass fit is forced to equal the contribution from the incoherent and coherent process in the fit to the p_T distribution. In this way, the correlation between the yield parameters was broken, and the contribution from the three process were made independent of each other.

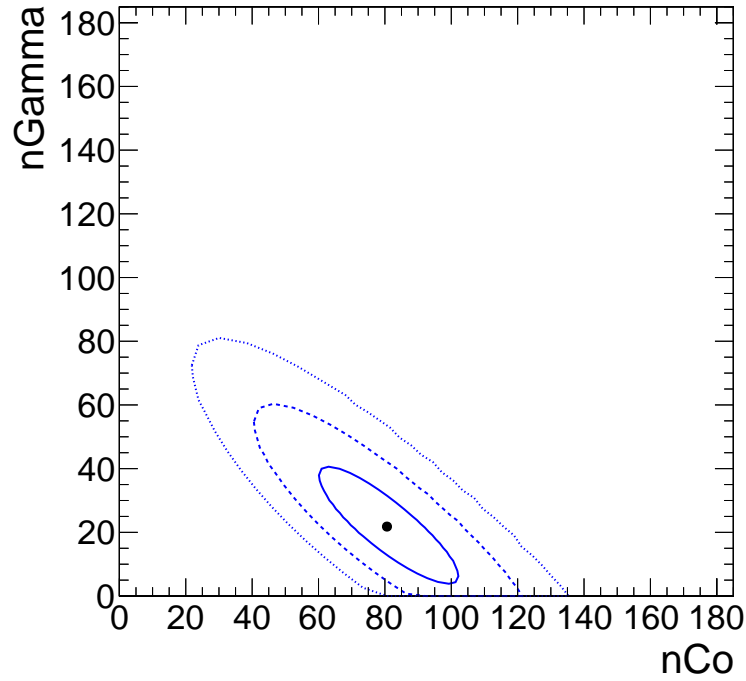


Figure 3.10: 68%, 95%, and 99% confidence contours from the p_T template fit.

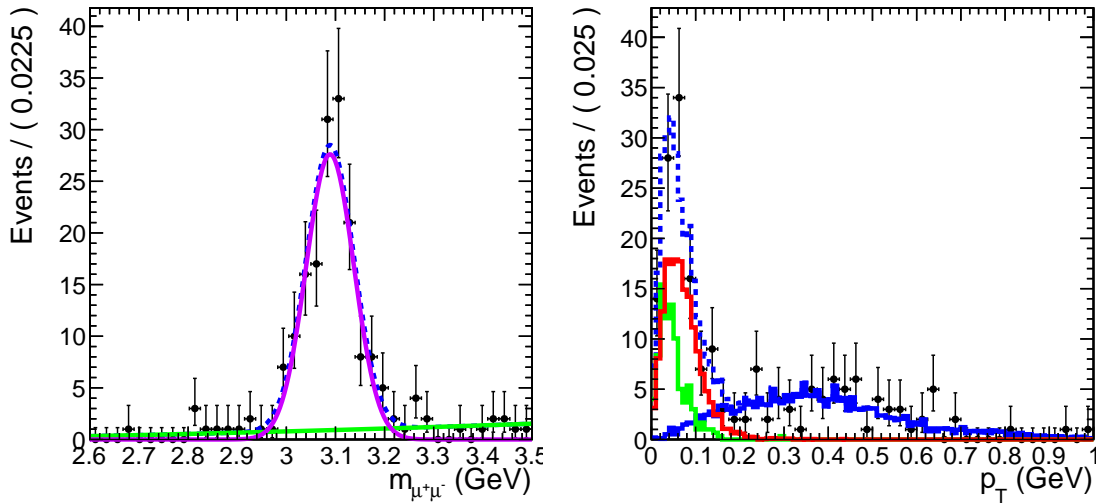


Figure 3.11: Simultaneous fit to the mass and p_T spectra.

622 The ambiguity between the coherent and incoherent processes in the mass fit and the ambiguity
 623 between the coherent and the photon-photon process was over come through used of the simultane-
 624 ous fit. Fig. 1.12 shows the confidence contours for nCo and $nGamma$ from the simultaneous
 625 fit. Fig. 1.11. The slope of the confidence contours in Fig. 1.12 is noticeably closer to 0 than the appar-

ent negative slope in Fig. 1.10. The contours for the simultaneous fit are also reduced compared to Fig. 1.10 with widths in nCo and $nGamma$ similar to those expected from Poisson statistics. From the simultaneous fit, reasonable statistical errors were obtained along with the yields for the three processes.

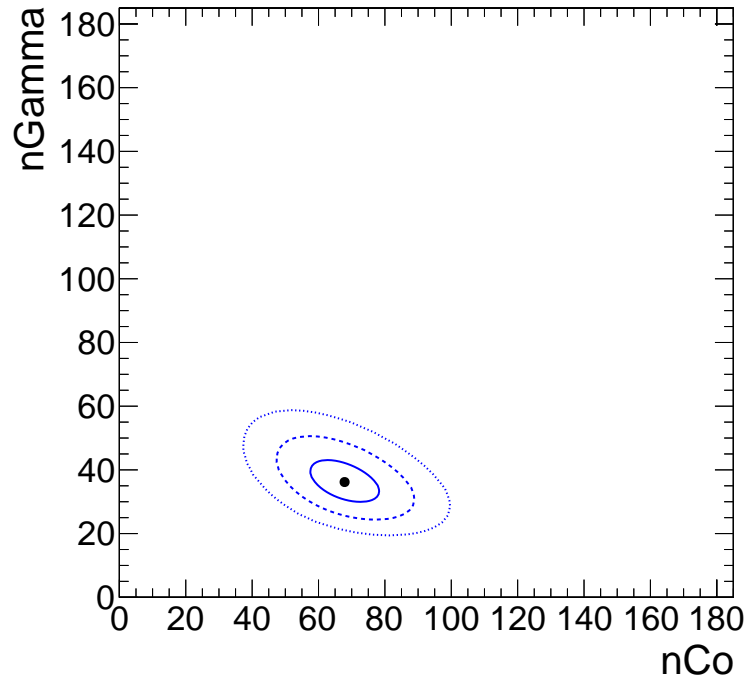


Figure 3.12: 68%, 95%, and 99% confidence contours from the simultaneous fit.

3.6 Efficiency determination

3.6.1 Muon efficiencies

The muon efficiencies are measured from MC and data. The MC based measurement accounts for the detector acceptance and the efficiency of the muon quality discussed in Section 1.3. The trigger efficiencies were measured in data using the tag and probe method [?], which is discussed below.

CMS has a limited acceptance for J/ψ s, particularly in the case of J/ψ s with low momentum like those produced in UPC events. To measure the acceptance of CMS for J/ψ s, reconstructed

dimuon candidates were considered detectable if both reconstructed daughters fell into a detectability region. This region was defined using the coherent J/ψ events obtained from STARlight. The efficiency for reconstructing single muons ϵ_{reco}^μ is defined by $\epsilon_{reco}^\mu = \frac{N_{reco}^\mu}{N_{gen}^\mu}$, where N_{reco}^μ is the number reconstructed muons obtained after the full CMS detector simulation and that passed the standard muon quality cuts, and N_{gen}^μ is the number of generated muons from STARlight. Fig. 1.13

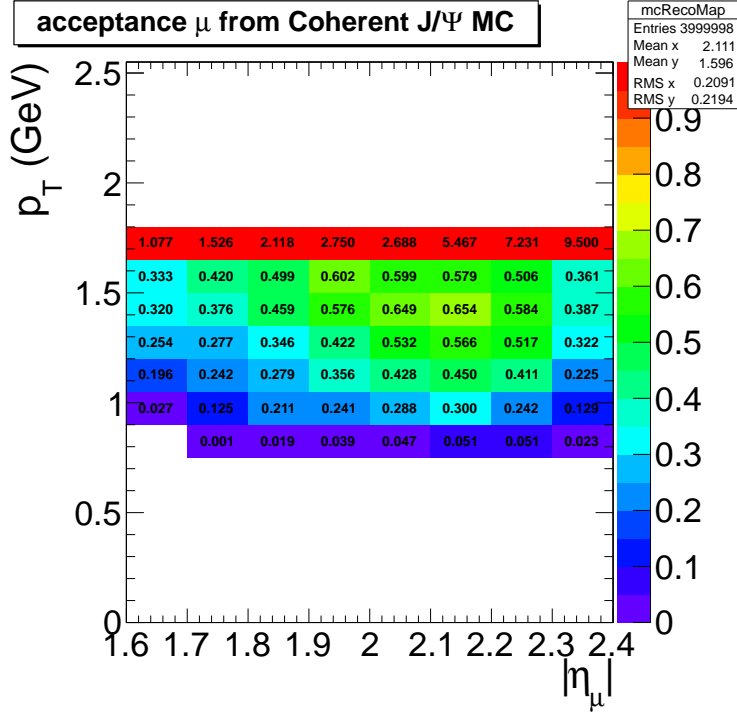


Figure 3.13: Muon daughter detectability from coherent J/ψ

shows the efficiency for reconstructing single muons from coherent J/ψ events. To avoid the edges of the detectors acceptance, all reconstructed muons that fall into a $(p_T, |\eta|)$ bin that has an efficiency less than 20% were rejected thus defining the detectability region. The acceptance for reconstructing dimuons was calculated from MC using the following formula:

$$A = \frac{N_{det}(|y|, p_T)}{N_{gen}(|y|, p_T)}, \quad (3.2)$$

where N_{det} is the number of reconstructed dimuons where both daughters fall into the detectability region, and N_{gen} is the number of generated dimuons. From Eq. 1.2, the acceptance for J/ψ was

calculated as a function of $|y|$, and p_T (see Fig. ??).

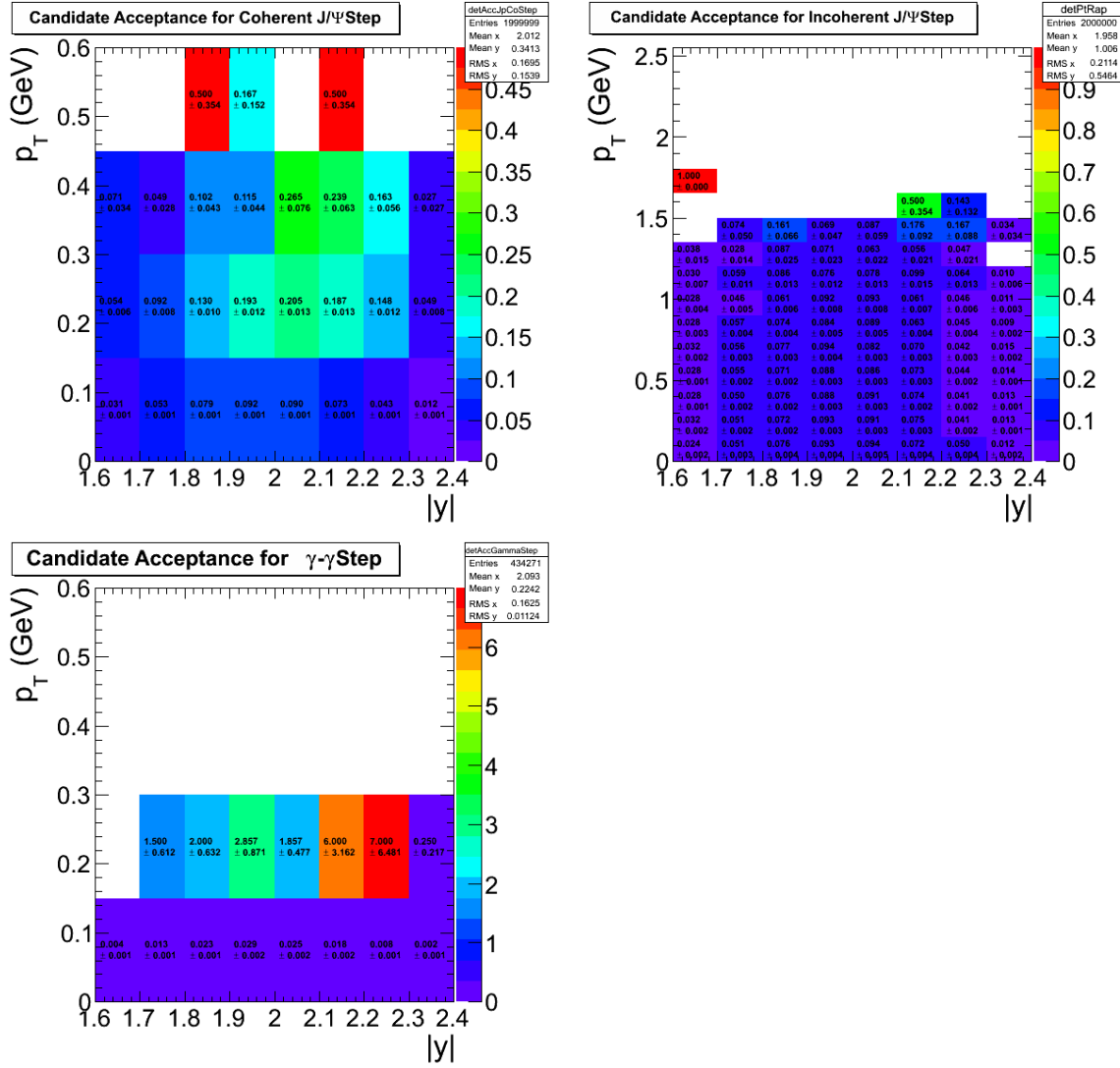


Figure 3.14: Dimuon acceptance from coherent J/ψ (top left), incoherent $J\psi$ (top right), and photon-photon interactions (lower).

The tag and probe method is used to measure the trigger efficiency of the muon daughters, which is a data driven approach. In this method there are three categories of daughter muons. *Tag muons* are high quality muons. *Passing probes* are reconstructed muons that match the muon trigger, while *failing probes* do not. Each dimuon will have one daughter classified as a tag and the other as a probe. From here three invariant mass histograms are studied. One histogram is created from all pairs. The second comes from pairs where the probe is a passing probe. The last

655 histogram comes from pairs where the probe fails to fulfill the trigger, *i.e.* the probe is a failing
 656 probe. Because this depends on the p_T and $|\eta|$ of the probe, one set of three histograms for each
 657 $(p_T, |\eta|)$ bin of the probe is created.

658 To extract the single muon trigger efficiency ϵ_{trig}^μ , each set of invariant mass histograms was
 659 simultaneously fitted. The signal was fitted using a Crystal Ball function, and the background
 660 was fitted to an exponential. The Crystal Ball parameters were simultaneously fitted to all three
 661 histograms. The exponential function was fitted to the failing and passing probe histograms sepa-
 662 rately. Because the background shapes are in principle different for the two samples, the efficiency
 663 is driven by this difference.

664 To measure the trigger efficiency a tag is required to pass all muon quality cuts and matched
 665 to the trigger. The probe is required to pass all quality cuts. A passing probe is a probe that is
 666 also matched to the trigger. In this way, the tag leaves the probe unbiased by the trigger and the
 667 efficiency can be measured by fitting the mass distribution.

Fig. 1.15 shows the fit of the three sets of pairs. This fit is done for each bin of the probes p_T

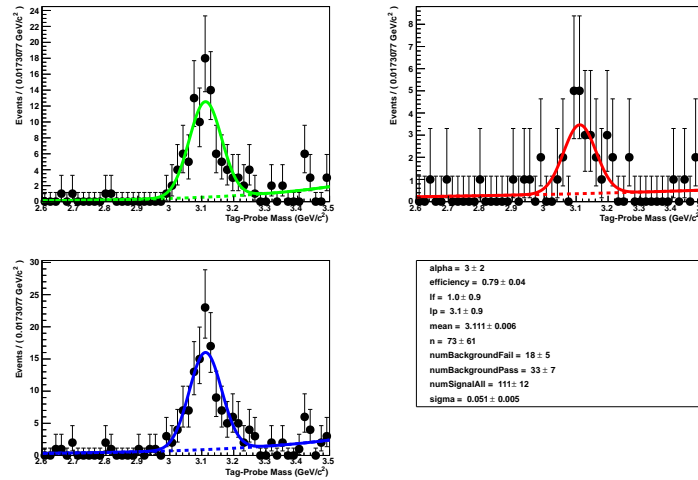


Figure 3.15: Fits to tag and probe pairs in the J/ψ mass region for pairs with a probe $2 < |\eta| < 2.2$ and $1.55 < < 1.8$ GeV.

668 and η . The resulting fit is in Fig. 1.16.

670 The dimuon trigger efficiency $\epsilon_{trigger}^{dimuon}$ was measured from the single muon efficiencies. The

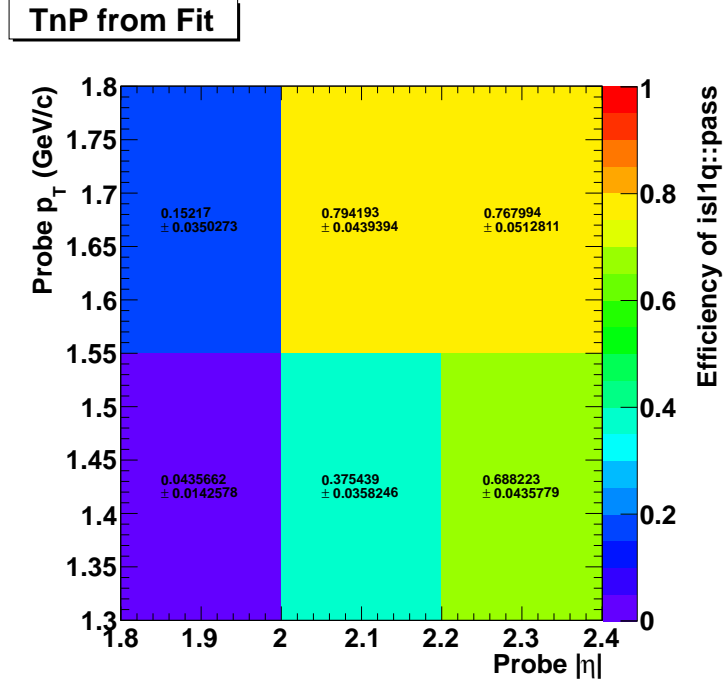


Figure 3.16: Muon trigger efficiencies in p_T and η bins from the tag and probe method.

671 efficiency of each candidate was calculated using the following equation:

$$\epsilon_{trigger}^{dimuon} = 1 - (1 - \epsilon_{trigger}^{\mu_1})(1 - \epsilon_{trigger}^{\mu_2}), \quad (3.3)$$

672 where $\epsilon_{trigger}^{\mu_1}$ is the tag and probe efficiency of the first dimuon daughter, and $\epsilon_{trigger}^{\mu_2}$ is the effi-
 673 ciency of the second muon daughter. In Eq. 1.3 the probability of at least one daughter firing the
 674 trigger is calculated by subtracting one from the probability that neither daughter fires the trigger,
 675 thus giving the dimuon trigger efficiency.

676 The average dimuon trigger efficiency for each dimuon ($p_T, |y|$) bin was calculated by average-
 677 ing the individual dimuon candidates in each bin. The average trigger efficiency was multiplied by
 678 the acceptance from the MC to produce a total factor for both efficiency and acceptance.

679 The total combined efficiency and acceptance factor coherent J/ψ between $2.0 < |y| < 2.2$ was
 680 found to be around 5%. The roughly 7% acceptance factor from the MC is the main contributor
 681 to the total efficiency. Primarily, the interplay of the polarization of the J/ψ and the material in

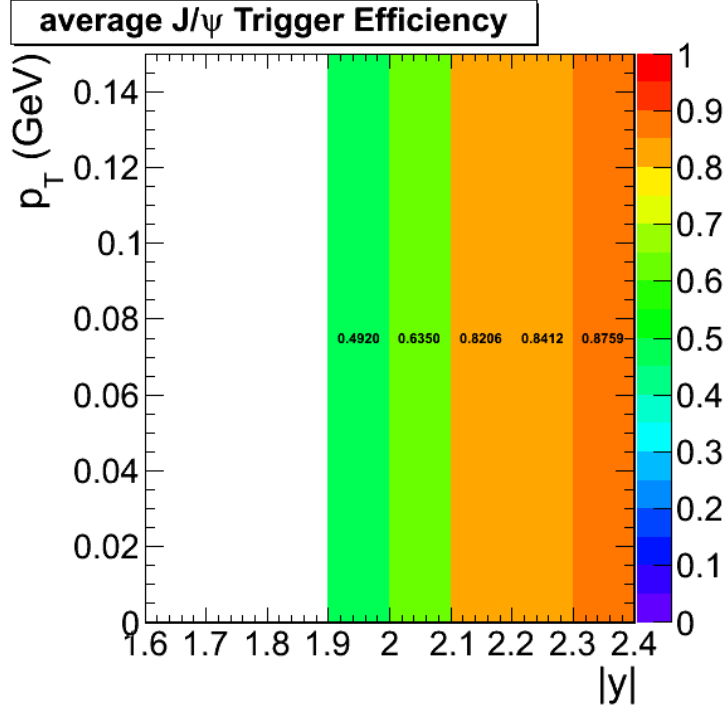


Figure 3.17: The trigger efficiency from tag and probe averaged over candidates in each $(p_T, |y|)$ bin.

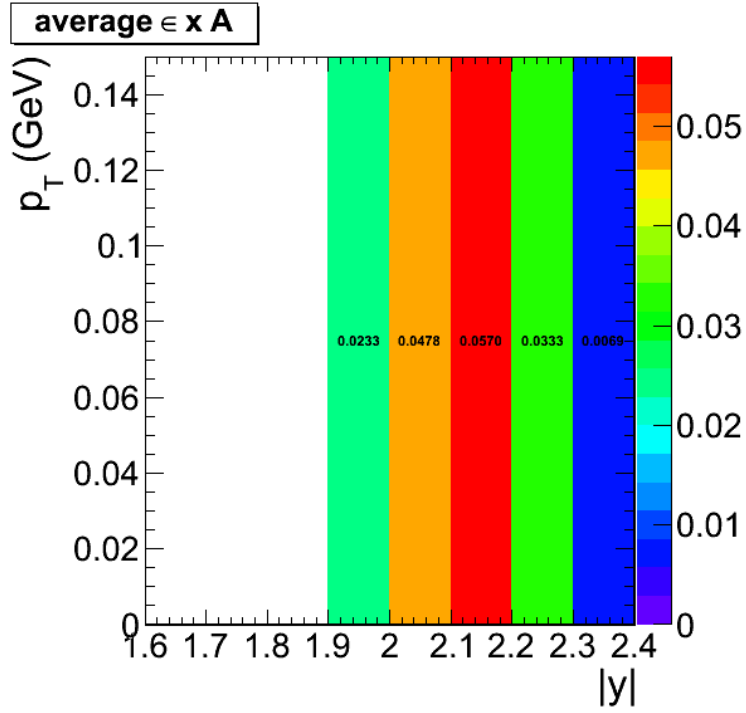


Figure 3.18: The acceptance times averaged trigger efficiency from tag and probe.

detector drive down the efficiency by creating an effective momentum threshold for detection (see Section 1.1). The reconstruction efficiency of the daughters range between 20%-60% for muons in the defined detectability range. The trigger efficiency for the detectable muons ranges from 30%-80% depending on p_T . The typical trigger efficiency for the dimuons ranges from 60% to 80%.

3.6.2 ZDC trigger efficiency

As discussed in Section 1.4, a special trigger was prepared to monitor the ZDC trigger efficiency. This trigger required either a ZDC^+ or ZDC^- trigger, together with at least one pixel track. Events were accepted offline if there was no activity in the BSCs or activity on a single side.

This sample suffers from a trigger bias. For example, a sample triggered by ZDC^+ would always produce a ZDC^+ trigger efficiency of one. To avoid this, the special trigger sample was divided into two subsamples in the following way. A first sample triggered by the ZDC^+ input and second one triggered by the ZDC^- . The ZDC^+ trigger efficiency is measured from the ZDC^- sample, and vice versa.

The trigger efficiency for reconstructed ZDC energies above the single neutron threshold were estimated (see for Sec. 1.4). The ZDC^+ efficiency was calculated using the ZDC^- triggered sample. To estimate the efficiency, the number of events with energy in ZDC^+ greater than the single neutron threshold, N_{events} , were measured. From this set of events, the number of events that also fire the ZDC^+ was measured. The ratio between the number of single neutron events that fired the trigger and all single neutron events was taken as the estimate of trigger efficiency. The same procedure was applied for each side of the ZDC. The trigger efficiency of the ZDC was found to be 98% for ZDC^- and 94% for ZDC^+ .

ZDC Side	Reco Method	N_{events}	N_{trig}	ϵ_{ZDC}
ZDC ⁺	1	72946	71688	0.982 ± 0.005
ZDC ⁺	2	73028	71706	0.9819 ± 0.005
ZDC ⁻	1	76137	71786	0.9429 ± 0.005
ZDC ⁻	2	76132	71859	0.9439 ± 0.005

Table 3.5: ZDC trigger efficiencies for ZDC reconstruction method 1 and 2

3.7 Systematic checks

Table 1.6 shows the systematic errors that were estimated. The method used to separate the coherent from the photon-photon process is the most dominant error. The ZDC reconstruction method used to estimate the neutron thresholds is the next most dominant, followed by the method used to estimate the HF noise threshold.

systematic	uncertainty in %
Template fit normalized	+9.5% -12%
ZDC reconstruction	2.9%
ZDC trigger efficiency	2.2%
HF noise threshold	+1.3% -3.4%
MC acceptance	1.1%
Total systematic	8.1%

Table 3.6: Summary of systematic uncertainties

3.7.1 HF noise threshold

The way in which the HF noise distribution is measured affects the event selection and therefore the final candidate yield. This cut plays a significant role in rejecting hadronic events. In Table 1.4 the importance of cutting on HF noise is evident. The HF noise cut rejects a little less than 1/5 of the remaining events. The systematic uncertainties on the HF noise requirement is important for this reason. The result must not depend significantly on the method used to apply the cut on the noise because of the large reduction of events that result from it.

Four different approaches were employed to estimate the systematic effect arising from picking

a particular method for setting the HF noise threshold. By looking at the variation of the number of events that remain after applying the thresholds derived from these four methods, the systematic uncertainty for the HF noise cut was estimated. The four methods are derived from combinations of two variations. The type of object was varied from a low-level detector object called a RecHit to a higher level physics object called a CaloTower. The RecHit is the energy deposited in a single calorimeter detector element, whereas the CaloTower is a collection of RecHits with various thresholds, which represent a full energy deposit that would come from a particle or a collection of particles from a jet passing through the detector. The second variation is on the separation of the two sides. In one case the threshold is derived for the two sides combined. In another case the thresholds are calculated separately for the two sides of HF. By combining these two variations, a total of four estimates of the effect of the HF noise cut were made. Table 1.7 below shows the thresholds that are measured for each of the four methods. The resulting yields from the four different methods are displayed in Table 1.8.

Object type	HF (GeV)	HF ⁻ (GeV)	HF ⁺ (GeV)
RecHits	3.85	3.25	3.45
CaloTowers	4.25	3.25	3.75

Table 3.7: HF noise thresholds for various noise measurement methods.

Object type	Combined HF threshold	Two-sided thresholds
RecHits	298	290
CaloTowers	302	288

Table 3.8: Candidate yields below 1.05 GeV p_T for various HF noise cuts.

The threshold was adjusted to estimate the effect of tightening the requirement on the zero bias data. By successively lowering the percentage of the zero bias sample that was included, the HF noise cut was made more restrictive including first 98%, then 97% of all zero bias events. This was done for both object types, RecHits and CaloTowers. This allows for an estimate of the systematic uncertainty on selecting a 99% cut. Table 1.9 shows the effect on the thresholds themselves for both RecHits and CaloTowers, whereas Table 1.10 shows the effect on the candidate yields.

Table 3.9: Values of the energy cuts for the HF calorimeter for RecHit and CaloTower in GeV.

%	E_{RecHit} GeV	$E_{CaloTower}$ GeV
99	3.85	4.25
98	3.25	3.75
97	2.95	3.25

Table 3.10: Number of dimuon candidates with $p_T < 1.05$ when changing HF calorimeter cuts for RecHit and CaloTower.

%	RecHit cut	CaloTower cut
99	298	302
98	287	294
97	284	280

The systematic uncertainty in the HF noise threshold measurement was calculated taking the difference from the 99% combined RecHit method with the upper and lower extrema. The systematic uncertainty from this method is calculated to be +1.3% -3.4%.

3.7.2 Template fit normalization

The p_T template fit depends on the functions chosen for the fit to the mass distribution. As described in Section 1.5, the similarity of the of the p_T distribution for the coherent and photon-photon process make the contributions from the two process difficult to separate from the p_T distribution alone. The mass distribution was used to distinguish between these two processes. In turn, the p_T becomes dependent on the mass fit.

The systematic uncertainty due to the choose of functions used to fit the mass distribution was estimated by varying the signal and background functions. The contribution to the background from the mass fit was used to fix the contribution from the photon-photon process in the p_T template fit. Two functions were used to describe the signal, a Gaussian, and a Crystal ball function. The background was fit to a linear function, a 2nd order polynomial, and a 2nd order Cheby-Chev polynomial. The resulting variation on the coherent contribution was used to as an estimate of this systematic effect.

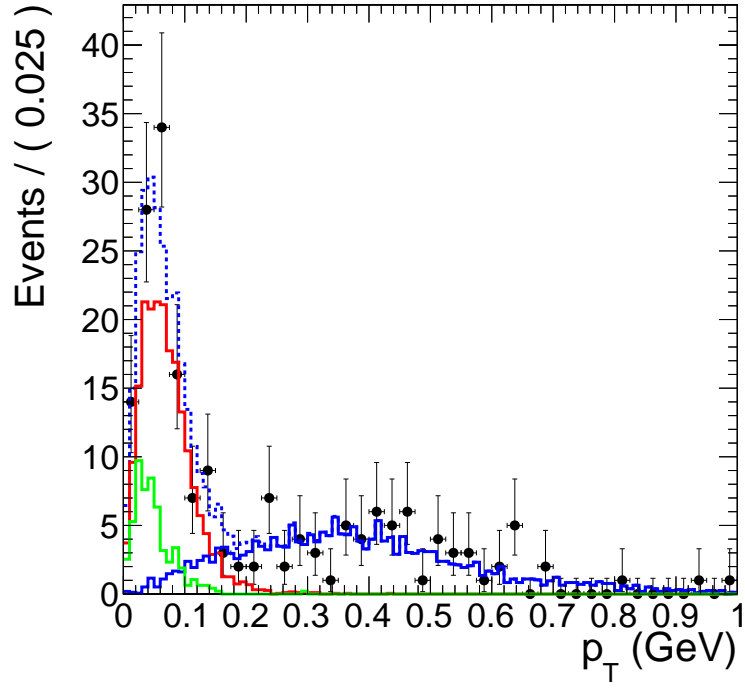


Figure 3.19: Coherent, incoherent, and photon-photon process p_T template fit to data.

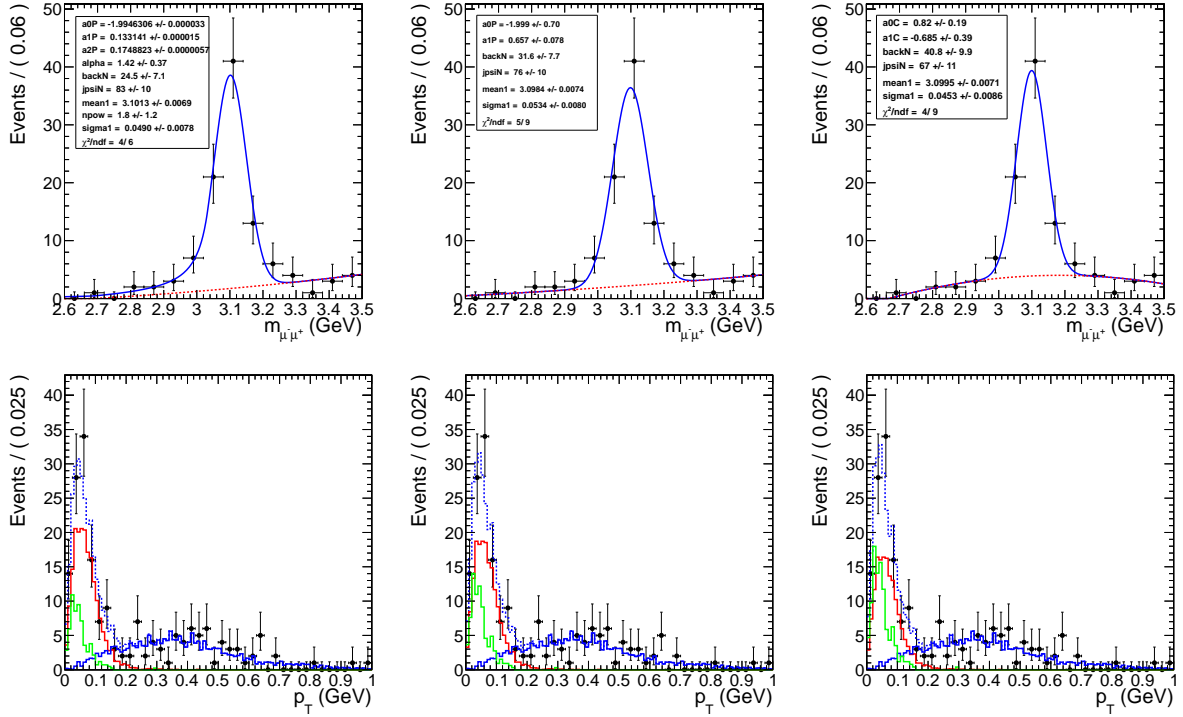


Figure 3.20: Various mass distribution fits and the corresponding p_T template fit.

Moving from left to right in Fig ??, the contribution from the photon process increases. The χ^2 pre degree of freedom is similar between the three fits indicating a similar goodness of fit. On this basis, neither fit is preferred. The left most fit uses a Crystal Ball function to account for the radiative decay of the final state daughters of the J/ψ . The low mass exponential portion however picks up background events and overestimates the J/ψ contribution. The right most plot fits the background to a 2nd order Cheby-Chev polynomial. Because the Cheby-Chev peaks just below the J/ψ peak, this fit overestimates the background and in turn underestimates the signal contribution. The Gaussian fit with a linear background however does a reasonable job of fitting both the background and the signal.

From these three fits an upper and lower bound of the systematics due the choice of fit functions was estimated. The difference between the Gaussian-Linear fit and the Crystal Ball-polynomial fit was taken as an upper bound. The difference between the Gaussian-Linear fit and the Gaussian-Cheby-Chev fit was taken as a lower bound. The overall systematic uncertainty due to the choose of mass fit functions is found to be +9.5% -12%.

3.7.3 Mass fit

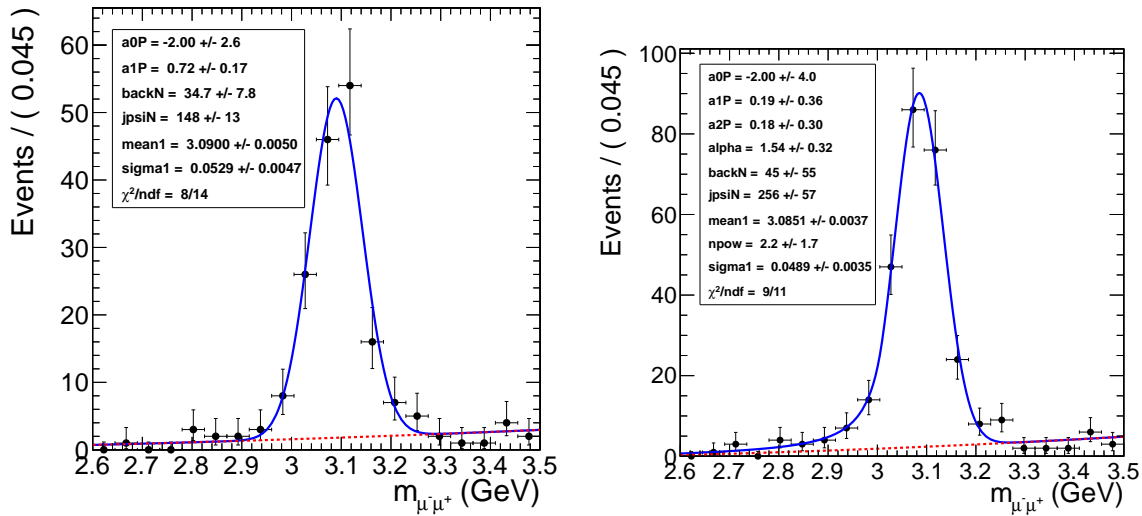


Figure 3.21: Mass fit to J/ψ using Gaussian (Left) and Crystal Ball (Right) for the signal and a polynomial for the background

Fig. ?? demonstrates the small dependence the raw J/ψ yield has on the fitting function. Both fit functions agree well, with reduced χ^2 values below one. The Crystal ball fit give an upper estimate for the J/ψ yield. The Gaussian fit gives an lower estimate. The main difference comes from the lower mass tails. In the Crystal ball fit the lower tail is considered to be signal due to shifting of the mass spectrum to lower mass due to radiation from the final state muons. In the Gaussian fit the lower mass tail is considered to be background and the signal is sharper.

As check on the simultaneous p_T and mass fit, the mass fit is done using mass templates from STARlight.

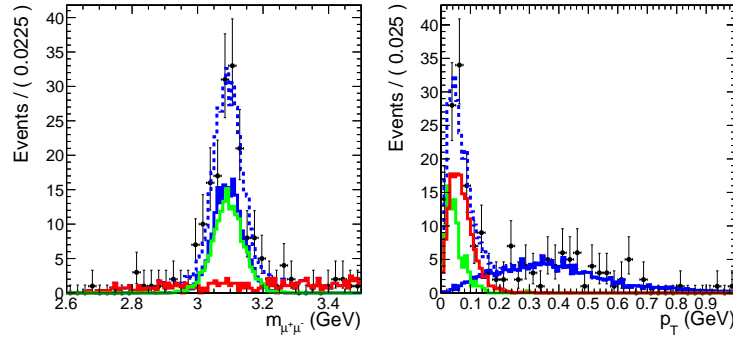


Figure 3.22: Simultaneous fit to the mass and p_T using mass templates for the mass fit.

3.7.4 MC acceptance

The MC derived acceptance correction factors depend on the input physics generator. The underlying p_T distribution was assumed to be correctly described by STARlight for the coherent cross section measurement. To estimate the effect of changing the underlying p_T distribution on the acceptance measured from the MC, the incoherent sample was used to correct the coherent yield. By using the broader p_T distribution of the incoherent process, an estimate of acceptance measurements dependence on the assumed shape of the p_T distribution was obtained. The systematic uncertainty due to the dependence of the acceptance correction on the p_T distribution of the input physics generator was estimated by the difference between the correction factors from the coherent and incoherent MC samples. Half the difference was used as the estimate and was found to be

785 1.1%.

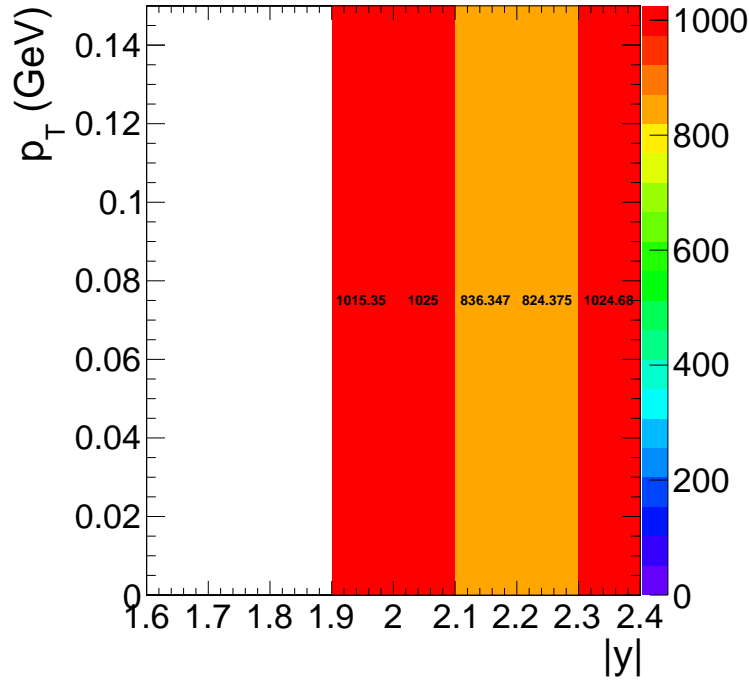


Figure 3.23: Yields corrected by the MC incoherent acceptance map.

786 The effect of polarization was estimated by correcting by the acceptance for an unpolarized
 787 J/ψ sample.

788 3.7.5 ZDC reconstruction

789 An additional method for estimating the ZDC neutron thresholds was used to estimate the sys-
 790 tematic errors on the threshold measurements. This additional method, used in previous ZDC
 791 measurements, differs in the way the signal time slices are used to calculate the signal from each
 792 channel. In the standard method, the signal is taken from the sum of time slices 4, 5, and 6. To
 793 estimate the event by event noise pedestal the sum of time slice 1 and 2 are used. The signal for
 794 an individual ZDC channel is then calculated as the sum of the signal time slices minus the sum
 795 of the noise time slices weighted by a factor of 3/2 to account for the differing number of noise
 796 versus signal time slices. The advantage of the standard method is that by using multiple signal
 797 and noise time slices the signal and noise are effectively averaged reducing time slice to time slice

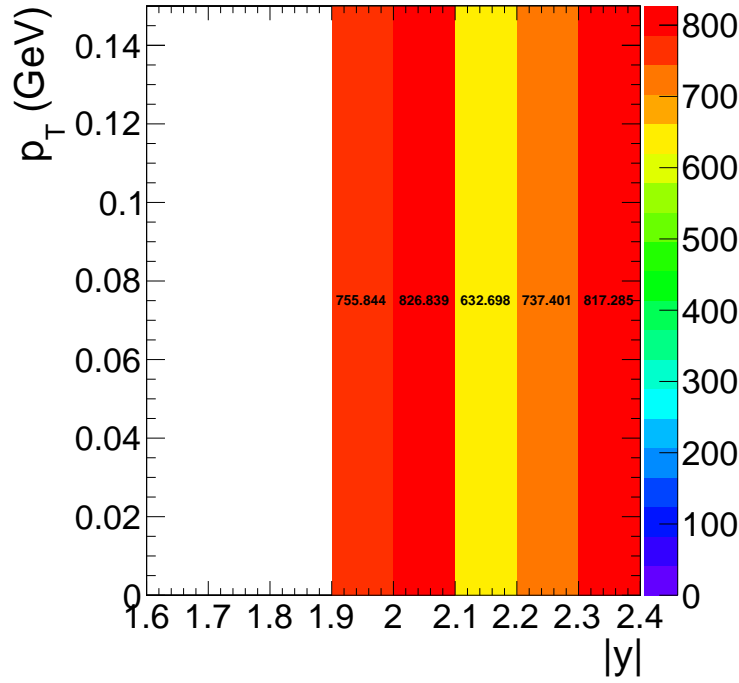


Figure 3.24: Yields corrected by an unpolarized J/ψ sample.

fluctuations. However, by using time slices 1 and 2 for measuring the noise, the noise can only be measured half the time due to unmeasurable negative fluctuations of the dominant low frequency component of the noise.

As in the new method described in Section 1.4, the standard method combines the channels to create a signal measurement from the whole of each side of the ZDC, one measurement for ZDC^+ , and one for ZDC^- . The noise subtracted signal from each of the HAD channels are added together. Then the EM section channels are summed. The EM section is weighted by a factor of 0.1 as in the new method. After the weighting the EM and HAD channels are added to each to create one measurement for ZDC^+ and another measurement for ZDC^- .

Fig. ?? shows the spectra for ZDC^+ and ZDC^- using the standard method. The same fit used for the new method is applied to standard method. As in the new method, the single neutron threshold is set to 2σ below the mean from the fit to the one neutron peak. The multi-neutron threshold was set to 2σ above the one neutron peak.

The systematic uncertainty due to the ZDC reconstruction method are estimated from the dif-

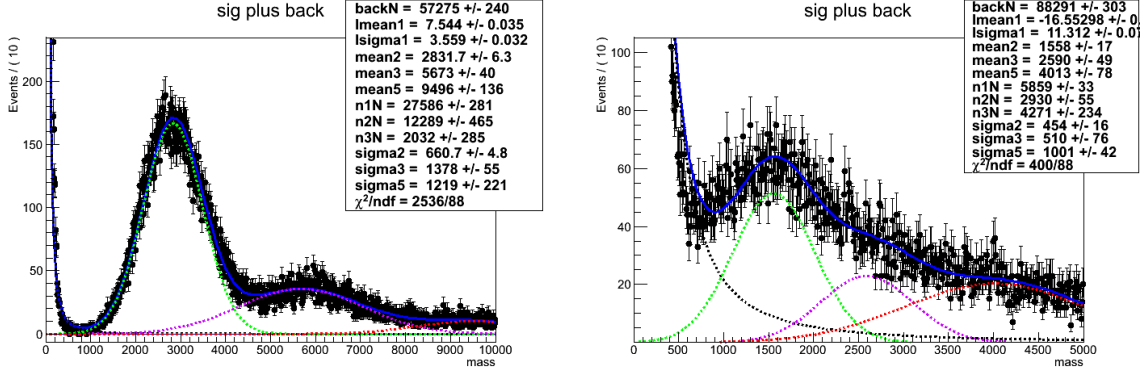


Figure 3.25: Fit to charge spectrum from ZDC⁻ (left) and ZDC⁺ (right) using the standard reconstruction method

ference between the UPC J/ ψ candidate yields. Both the reconstruction method and thresholds were changed to calculate the effect of the reconstruction method. The yields for the new and standard ZDC reconstruction method in the Xn0n break up were found to be 298 and 315 respectively. Half the difference between the two methods was used as an estimated of the systematic uncertainty. The systematic uncertainty due to the ZDC reconstruction method was found to be 2.9%.

3.7.6 ZDC trigger efficiency

The ZDC trigger efficiency measurement is sensitive to the underlying neutron distribution. The more neutrons that high the ZDC the higher the trigger efficiency will be. To estimate the effect the input sample has on the efficiency, the ZDC trigger efficiency was measured from five different samples. The Table 1.11 shows the results from the five samples. Both the new and standard ZDC reconstruction methods are shown for comparison.

The amount of electronic noise in the sample also effects the measurement. The more noise sits below the one neutron peak, the worse the efficiency is. In Table 1.11, the Zero Bias sample compared the Zero Bias sample with the timing cuts the described in the previous section shows a significant increase in efficiency in the sample with reduced noise. The same increase is seen when comparing the ZDC triggered sample with the ZDC triggered sample that also requires a

ZDC Side	Reco Method	N_{events}	N_{trig}	ϵ_{ZDC}
(ZDC ⁺ or ZDC ⁻) and 1 pixel track				
ZDC ⁻	1	72946	71688	0.982 ± 0.005
ZDC ⁻	2	73028	71706	0.9819 ± 0.005
ZDC ⁺	1	76137	71786	0.9429 ± 0.005
ZDC ⁺	2	76132	71859	0.9439 ± 0.005
(ZDC ⁻ or ZDC ⁺), 1 pixel track, and L1 EG trigger				
ZDC ⁻	1	613758	602123	0.9810 ± 0.0018
ZDC ⁻	2	614014	601863	0.9802 ± 0.0018
ZDC ⁺	1	643905	602671	0.9360 ± 0.0017
ZDC ⁺	2	647888	603089	0.9309 ± 0.0017
(ZDC ⁻ or ZDC ⁺), 1 pixel track, and L1 Muon trigger				
ZDC ⁻	1	65466	63376	0.9681 ± 0.0054
ZDC ⁻	2	65543	63358	0.9667 ± 0.0054
ZDC ⁺	1	71929	63512	0.8830 ± 0.0048
ZDC ⁺	2	72932	63582	0.8718 ± 0.0047
Zero Bias with ZDC timing cuts				
ZDC ⁻	1	88676	84429	0.9521 ± 0.0046
ZDC ⁻	2	88480	84202	0.9517 ± 0.0046
ZDC ⁺	1	59878	54728	0.9140 ± 0.0054
ZDC ⁺	2	60467	54733	0.9052 ± 0.0053
(ZDC ⁻ or ZDC ⁺)				
ZDC ⁻	1	30986	30333	0.9789 ± 0.0079
ZDC ⁻	2	31029	30339	0.9778 ± 0.0079
ZDC ⁺	1	39178	30164	0.7699 ± 0.0059
ZDC ⁺	2	35703	30443	0.8527 ± 0.0067
Zero Bias				
ZDC ⁻	1	109967	101598	0.9239 ± 0.0040
ZDC ⁻	2	110230	101561	0.9214 ± 0.0040
ZDC ⁺	1	253241	86660	0.3422 ± 0.0013
ZDC ⁺	2	156336	87401	0.5591 ± 0.0024

Table 3.11: ZDC trigger efficiencies for ZDC reconstruction method 1 and 2 for different trigger samples

pixel track. The effect of the electronic noise is also present in the difference seen in using the two methods. As seen in Fig. 1.26, the new reconstruction method shows better separation of the one neutron peak from the electronic noise, in particular in ZDC^+ where the signal gain is lower. For this reason, the Zero Bias data, which contains that largest contribution from electronic noise, shows the most separation between the two methods and give the lowest estimate for the ZDC trigger efficiency.

The systematic uncertainty due to the uncertainty in the underlying distribution was estimated by calculating the standard deviation of the least extreme values from Table 1.11. Any value greater than three standard deviations from the mean was thrown out.

3.7.7 ZDC reconstruction method comparison

The new method relative to the standard method separates low signal from the noise more effectively for both sides of the ZDC. This is particularly important for ZDC^+ where the 1st HAD section had a lower gain than the other sections. The ZDC^+ and ZDC^- signals near the one neutron peak using the standard and new reconstruction methods were plotted for comparison in Fig. 1.26. In Fig. 1.26, the shrinking of width of the noise peak around zero in the new method versus the old

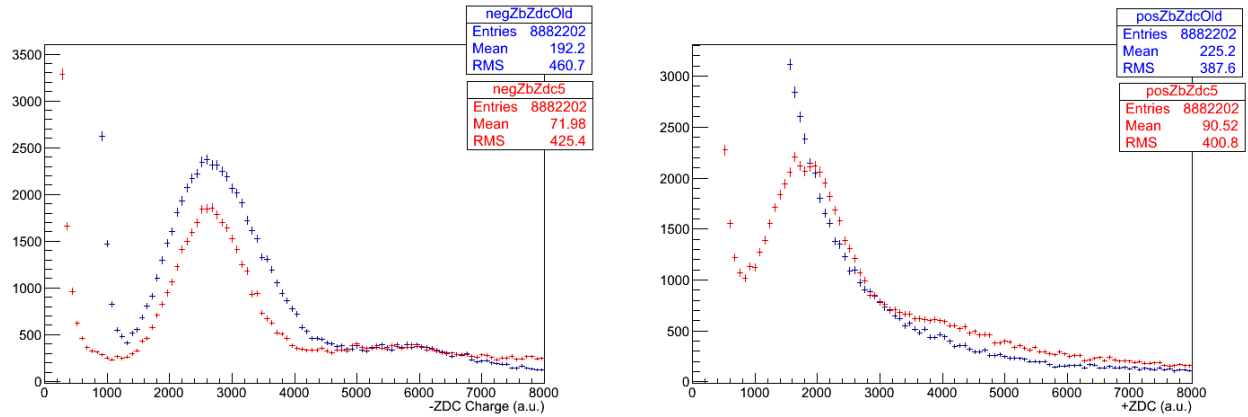


Figure 3.26: Comparison of the **new** ZDC reconstruction method and the **standard** method for ZDC^- (left) and ZDC^+ (right).

method is apparent for both ZDC^+ and ZDC^- . For the standard method no single neutron peak is resolved in ZDC^+ , whereas the single neutron peak is resolved using the new method.

Timing cuts were applied to enhance the signal relative to the background in order to resolve the one neutron peak in ZDC^+ using the standard method. Because the products of the collision are synced with time slice 4, noise can be rejected by selecting channels where the maximum signal falls into time slice 4. The noise will have no preferred time slice (see Fig. 1.4). Using this fact, signal can be preferably selected by requiring that the hadronic channels of the ZDC have a peak signal in the fourth time slice. Through these timing cuts the single neutron peak was recovered using the standard reconstruction for ZDC^+ .

To examine the effectiveness of the timing cuts, event by event noise subtraction was removed from the standard reconstruction. The signal from each channel was taken from time slices 4,5, and 6 with out subtracting 1 and 2. The signal spectrum from ZDC^- was then plotted with the result shown in Fig. 1.27. As each additional hadronic channel is required to have a maximum

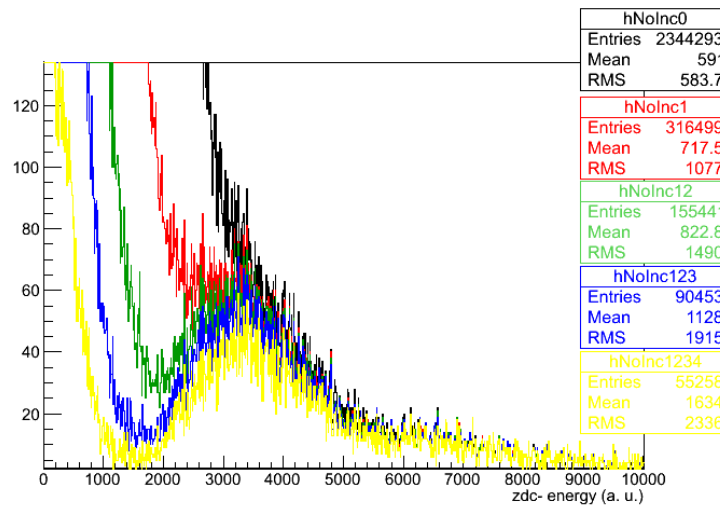


Figure 3.27: Effects of requiring in-time signal in successively more ZDC hadronic channels, no timing, at least **one**, at least **two**, at least **three**, and all **four** HAD channels have a maximum signal in the fourth time slice.

signal in the fourth time slice, the single neutron peak emerges. Fig. 1.27 demonstrates that the single neutron peak can be recovered from the noise using timing cuts alone.

Using the standard noise subtraction method, the same signal that emerges from the timing cuts alone appear without timing cuts. Fig. 1.28 confirms that both noise subtraction and the timing requirement produce the same signal. This gives confidence that the signal is not an artifact

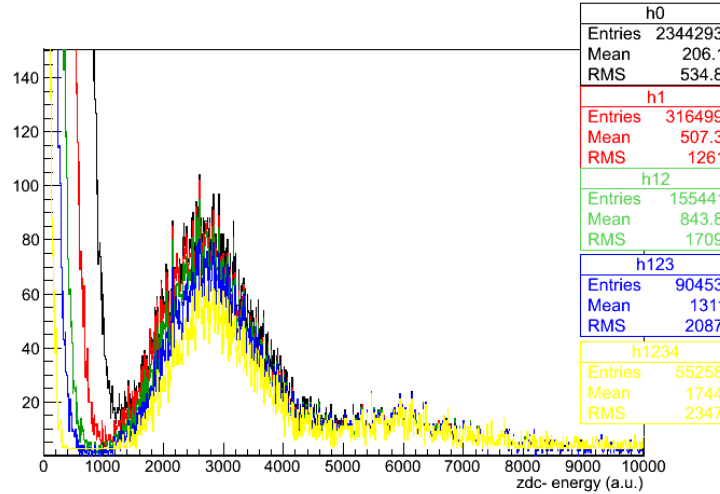


Figure 3.28: Effect of ZDC signal timing requirements after noise subtraction.

of either cut, but the true neutron signal.

Fig. 1.28 and Fig. 1.26 demonstrate the consistence of the using timing cuts and noise subtraction to enhance the signal neutron peak. Fig. 1.28 confirms the legitimacy of the timing requirement method in ZDC^- by showing the that the same signal emerges from the noise subtraction method as the timing method. Fig. 1.26 demonstrates the corresponds between the new noise subtraction method and the standard method on in ZDC^- where signal is better separated from the electronic noise. This allows for confidence that the signal seen in ZDC^+ using the new method is the one neutron peak.

3.7.8 Tag and probe

The main purpose for fitting the mass spectra to estimate the efficiency is to separate the background from true signal. The background may not have the same efficiency as the signal, so separating the two is important if this is the case. In the tag and probe fit the signal peak from the J/ψ resonance is fit to the probes, passing probes, and failing probes alike (see Fig. 1.15). The signal shape, if from the same physical signal, will be identical in each of the three distributions. The background is for the passing and failing probes is fit using different parameters for the background because the background may come from different physical processes than the sig-

nal or non-physical sources like combinatorial backgrounds or misidentified fake particles. When the background comes from sources other than the physical signal, the background may give an efficiency estimate that is lower than the signal.

The trigger efficiency measured by the tag and probe method depend on the fitting functions use to estimate the background and signal contributions. Depending on what functions is used to fit the spectra, the amount of amount of background can be over or underestimated and effect the efficiency measurement. To estimate this effect, the tag and probe efficiencies were additionally measured by counting probes in the J/ψ mass window. The whole mass window is used to estimate the efficiency including all the events from the mass side bands. In this way, a worst case scenario estimate is given where all background events are included as signal.

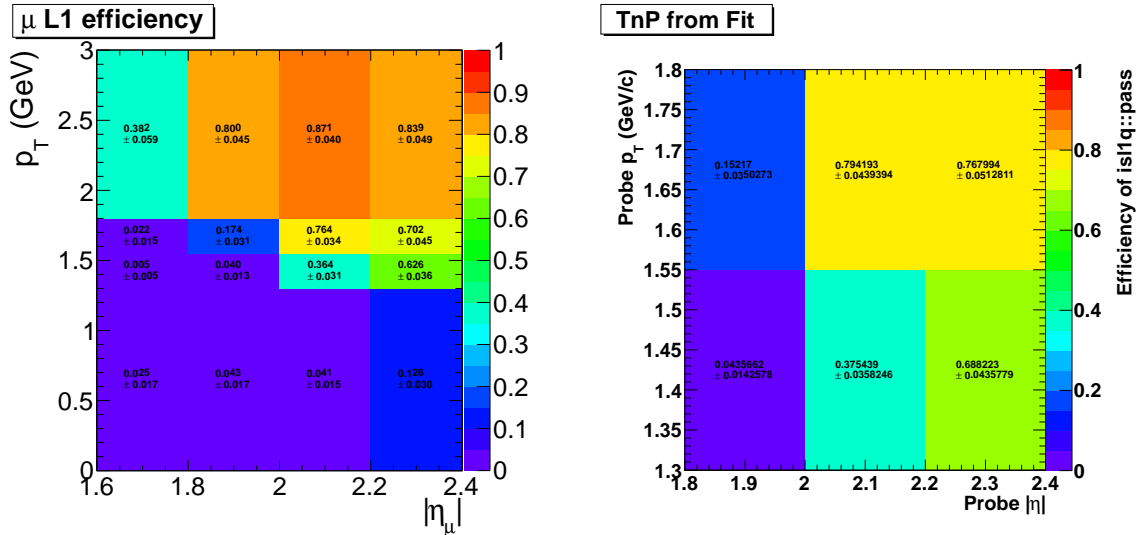


Figure 3.29: Tag and probe trigger efficiencies from counting (left) compared to fitting (right)

From Fig. ?? it is apparent that the choice of fit function and therefore the amount of background from the mass side bands is included in the signal measurement has very little effect on the tag and probe efficiency measurement. The small effect of including the side bands is due to the side bands being comprised mostly of photon-photon events. Because this background is neither decays from other particles like pions nor is it non-physical background like combinatorics, the efficiency for muons from the sidebands are nearly identical to J/ψ signal. The photon-photon process directly produces two muons just like the J/ψ , therefore efficiency estimated from the side

bands has little effect on the measurement because of this similarity. The counting and fitting trigger efficiency measurements agree within statistical uncertainties, so this uncertainty was taken to be negligible.

3.7.9 MC vs Data compairson

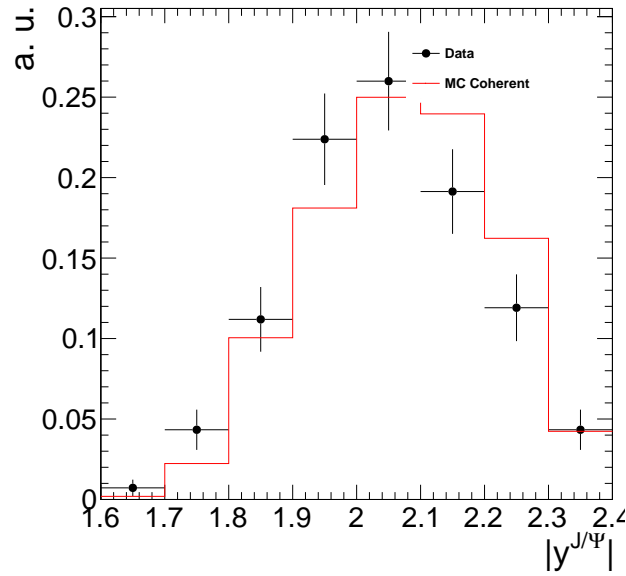


Figure 3.30: Comparison of the of the dimuon rapidity distributions between coherent MC sample and Data.

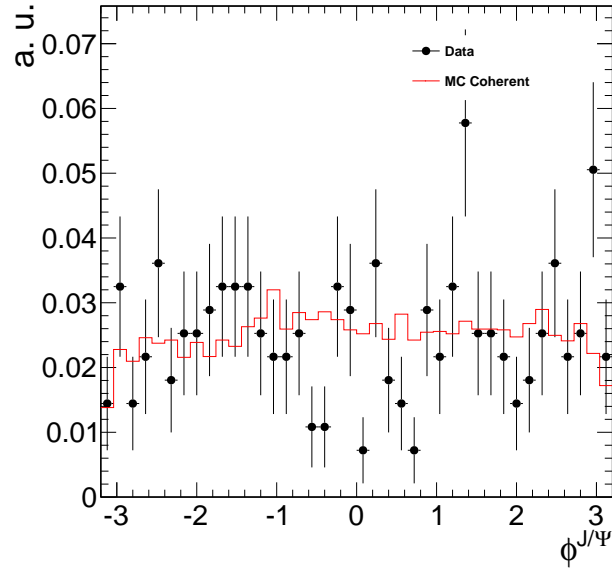


Figure 3.31: Comparison of the of the dimuon ϕ distributions between coherent MC sample and Data.

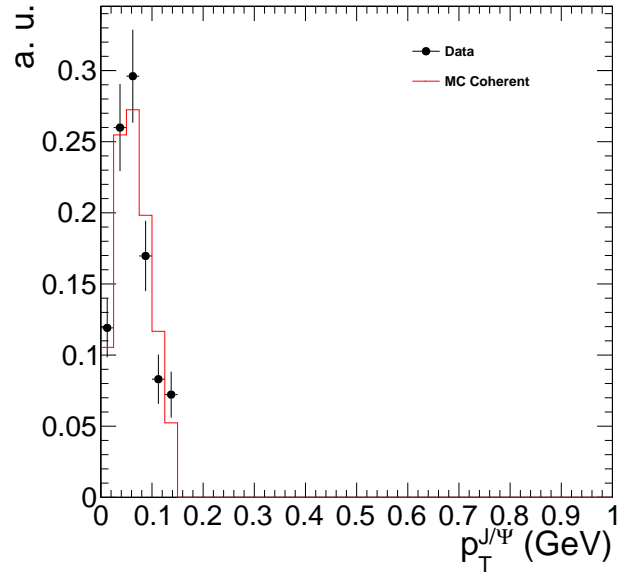


Figure 3.32: Comparison of the of the dimuon p_T distributions between coherent MC sample and Data.